

Poisson CNN: Convolutional Neural Networks for the Solution of the Poisson Equation with Varying Meshes and Dirichlet Boundary Conditions

Ali Girayhan Özbay*¹, Sylvain Laizet¹, Panagiotis Tzirakis², Georgios Rizos², and Björn Schuller²

¹*Department of Aeronautics, Imperial College London, Exhibition Rd, London SW7 2AZ, UK*

²*Department of Computing, Imperial College London, Exhibition Rd, London SW7 2AZ, UK*

November 20, 2021

Abstract

The Poisson equation is commonly encountered in engineering, including in computational fluid dynamics where it is needed to compute corrections to the pressure field. We propose a novel fully convolutional neural network (CNN) architecture to infer the solution of the Poisson equation on a 2D Cartesian grid of varying size and spacing given the right hand side term, arbitrary Dirichlet boundary conditions and grid parameters which provides unprecedented versatility in this application. The boundary conditions are handled using a novel approach by decomposing the original Poisson problem into a homogeneous Poisson problem plus four inhomogeneous Laplace sub-problems. The model is trained using a novel loss function approximating the continuous L^p norm between the prediction and the target. Analytical test cases indicate that our CNN architecture is capable of predicting the correct solution of a Poisson problem with mean percentage errors of 15% and promises improvements in wall-clock runtimes for large problems. Furthermore, even when predicting on meshes denser than previously encountered, our model demonstrates encouraging capacity to reproduce the correct solution profile.

Our results are fully reproducible: github.com/aligirayhanozbay/poisson_CNN_jupyter

Keywords: Convolutional neural network, Poisson equation

1 Introduction

Partial differential equations (PDEs) describe complex systems in many fields of engineering and science, ranging from fluid flows to options pricing. Despite their ubiquity, however, they can be very costly to solve accurately. One of the most important PDEs in engineering is the Poisson equation, expressed mathematically as

$$\nabla \cdot \left(\frac{1}{\rho} \nabla u \right) = f \quad (1)$$

Appearing in a diverse range of problems from simulating fluid flows, where it appears in the pressure field update step, to electrodynamics, the Poisson problem plays a central role in the design of many modern technologies. A variety of methods have been developed to solve the equation using numerical methods on regular grids, though all currently available methods come with drawbacks that can be potentially severe given the size of the mesh and the amount of resources available:

- Direct solution: Express the mesh node values as a linear system $\mathbf{A}\vec{u} = \vec{f}$, solve for \vec{u}
 - **Advantages:** Simple set-up, accurate

*Corresponding author. Email: ago14@ic.ac.uk

- **Disadvantages:** Prohibitively expensive for large problems due to $O(n^3)$ complexity (where n is the product of the mesh sizes across every dimension)
- Successive over-relaxation: Iteratively solve the system $\mathbf{A}\vec{u} = \vec{f}$
 - **Advantages:** Substantially faster than direct methods (complexity $O(n^2)$)
 - **Disadvantages:** Convergence is not guaranteed and can 'stall', generally lower accuracy
- Fast Fourier Transform: Transform the equation into wavenumber space to solve algebraically
 - **Advantages:** Fast (complexity $O(n \log n)$), very accurate (machine precision guaranteed)
 - **Disadvantages:** Only compatible with periodic boundary conditions
- Multigrid: Iteratively solve the problem using a number of successively coarser grids to eliminate low wavenumber error faster
 - **Advantages:** Very fast (theoretical complexity $O(n)$ per Lui [1])
 - **Disadvantages:** High memory requirements. Significant overheads and parallelization issues associated with the matrix operations in the restriction and interpolation steps which impact the theoretical time complexity.

Considering the drawbacks associated with these methods, a fast (preferably $O(n)$) and highly parallel way of approximating the solution of the Poisson equation would be a very powerful tool. Neural networks (NNs)¹ are well positioned to satisfy these criteria, having already been used in various areas of engineering and applied mathematics for complex regression tasks. Moreover, noting the recent strides in using fully convolutional models to perform image-to-image translation and the similarity of the Poisson problem to these tasks (with the source image(s) being the right hand side (RHS) and boundary condition (BC) terms, and the result being the solution), we chose to adopt a fully convolutional strategy to exploit the ability of such architectures to process large inputs of varying size efficiently.

Leveraging these strengths, our principal motivation is to develop a convolutional neural network (CNN) based Poisson equation solver that is able to match the capabilities of traditional (e.g. finite differences based) solvers. In this work specifically we present a novel CNN architecture capable of handling arbitrary RHS functions and Dirichlet BCs on rectangular 2D grids of variable size (with variable but uniform grid spacing), with the intended aim of incorporation of our model into traditional computational fluid dynamics (CFD) solvers simply as a drop-in replacement to the existing Poisson solver routines.

2 Related work

Interest in solving PDEs using NN-based methods has a relatively long history, beginning in the 90s with efforts by Hyuk and Kang [2], Dissanayake and Phan-Thien [3] and Lagaris et al. [4]. A significant proportion of early works on using NNs to approximate the solutions of PDEs focus on approximating the solution u given the variables it depends on, such as spatial coordinates, treating the NN as a continuous function. Training is performed to minimize the solution residuals inside the domain and on the boundaries. For example, Lagaris et al. [4] utilize a single layer perceptron (constrained due to the computational power limitations of the time) to augment trial functions known to satisfy the equation in question to solve a number of benchmark problems in numerical analysis, such as the Poisson equation subject to both (fixed) Dirichlet and Neumann BCs using various RHS functions.

This rather intuitive application of NNs greatly benefits from the differentiability of NNs via the backpropagation algorithm (described in greater detail in Appendix A) since it provides a very accurate method to compute the residuals. Combined with other factors such as the accurate results achieved for specific problems using relatively few parameters, the computational constraints of the era and the relative infancy of more advanced NN architectures in use today, this method became the dominant approach in the early attempts to bring the

¹Please see Appendix A for an introduction

fields of PDEs and NNs together, though suffering from the rather severe drawback of each set of trained weights being able to handle only a specific RHS function and set of BCs.

With the increase in computation power through the 2000s, more complicated models with more parameters and multiple layers became the norm. Smaoui and Al-Enezi [5] used the greater amounts of computational power available to investigate deeper models, utilizing multilayer perceptrons to predict the proper orthogonal decomposition modes of the 1D Kuramoto-Sivashinsky equation and the 2D Navier-Stokes equation. Baymani et al. [6] similarly used multilayer perceptrons to compute the solution of the Stokes equation by decomposing it into multiple Poisson problems and solving the Poisson problems with a procedure similar to the works discussed above. Furthermore, research into different neural computation methods began to garner attention, leading to works such as those using Radial Basis Function NNs by Li et al. [7] and by Mai-Duy and Tran-Cong [8]. A more detailed survey of the methods of the era was published by Kumar and Yadav [9].

Research into the applications of NNs to PDEs is still gaining significant momentum, driven by a number of factors providing a supporting ecosystem for deep learning research in general. Some of the most important factors are

- Substantial improvements in the hardware used to run NN training and inference, including in
 - GPGPU (General-purpose computing on graphics processing units) capabilities, delivering substantially greater FLOPS (Floating point operations per second) for 'embarassingly parallel' tasks compared to traditional CPUs (Central Processing Units)
 - Storage and memory capacity enabling much larger datasets and models
- Discovery of better practices to train NNs
- Substantial improvements in the availability of powerful, user-friendly, free and open source machine learning software to researchers such as Tensorflow [10] and Pytorch [11]
- A culture of making publications available in open-access repositories and releasing source code using free and open-source licences in the research community
- Explosive rise of interest in machine learning, data-driven methodologies and NNs in general catalyzed by the above factors

A brief overview of notable approaches being investigated in a modern setting may be found below.

2.1 Modern approaches on applying NNs to PDEs

The above factors led to great strides in models using the older, 'continuous' paradigm of training multilayer perceptron-style NNs to minimize solution residuals. Such models can now tackle a much greater variety of PDEs, solved in complex domains with a variety of BCs. A prominent example of advances in this area in recent times is the advent of 'Physics Informed Neural Networks (PINNs)' by Raissi et al. [12] who demonstrated the use of such a methodology to solve the Schrödinger and Burgers equations, the latter of which is of particular note due to the presence of a shock. Based on their paradigm, Lu et al. [13] developed the DeepXDE library, capable of solving a wide range of differential equations including partial- and integro-differential equations, providing a more user-friendly way of using NNs in this context. Furthermore, Meng and Karniadakis [14] proposed a method to help PINNs predict the correct values in a problem when given a combination of abundant yet less accurate 'low-fidelity' plus sparse yet more accurate 'high-fidelity' data.

Another subject that garnered substantial attention in the recent years is using NNs to 'discover' the underlying PDE describing e.g. a physical system from an existing dataset, typically set up such that the NN tries to find the numerical coefficients of a previously assumed PDE form by minimizing residuals. Notable examples include works by Long et al. [15], who adopted a convolutional methodology to first discover the coefficients for and then predict the time evolution of the 2D linear diffusion equation, and a number of works also by Raissi et al. [16] [17], with examples of applications to the Burgers' and Navier-Stokes equations among others. It is further

noteworthy that interest in this subject extends beyond the use of NNs, as evidenced by works such as those from Rudy et al. [18] using sparse regression.

Meanwhile, separate from the initial approaches to applying NNs to PDEs described above, fully convolutional models that capitalize on significant strides made in computer vision using CNNs began to gain traction. Utilizing common techniques in computer vision by treating the known terms and solutions of PDEs on rectangular meshes as though they were images, such methods approach the task of solving a PDE as an image-to-image translation problem similar to the pix2pix method by Isola et al. [19].

2.2 Usage of CNNs and applications to the Poisson problem

A significant proportion of the efforts to use CNNs to solve PDEs has focused on the Poisson equation, considering its status as a well-understood benchmark problem with applications in many fields.

In the fluid mechanics community, works of Tompson et al. [20] and Xiao et al. [21] pioneered the usage of CNNs to solve the Poisson equation. While both use their models within the framework of a complete CFD solver to simulate the motion of smoke plumes around objects, the architectures used and training methodologies are different. The former developed a model which takes a three-dimensional array containing the velocity divergence and geometry information on cubic $128 \times 128 \times 128$ grids while the latter adopt a multigrid-like strategy with multiple discretizations to make predictions on larger $384 \times 384 \times 384$ grids. Moreover, the former train the NN to minimize the divergence of the velocity field only while the latter adopt a more direct strategy by trying to instead minimize a linear combination of the L2 norms of the velocity divergence and the discrepancy between the predicted and ground truth pressure correction values by leveraging the additional data available from the specific methodology adopted.

Outside fluid mechanics, Shan et al. [22] investigated the application of a fully convolutional NN to predict the electric potential on cubic $64 \times 64 \times 64$ grids given the charge distributions and (constant) permittivities, claiming average relative errors below 3% and speedups compared to traditional methods.

In general, all of these works attempt to predict the solution of the Poisson equation given an array containing the values of the RHS function on a grid. However, they are all designed to make predictions for a specific application, on a specific mesh (with a particular resolution and grid spacing) and a specific set of BCs which greatly hinder the usefulness of the models in real world use cases since the models will need to be re-trained whenever any of these change. To overcome these limitations, using previous work as a starting point, we propose a fully-convolutional NN architecture that improves on the capability of previous models, adding support for

- Arbitrary Dirichlet BCs
- Variable grid spacing
- Variable mesh sizes

3 Boundary condition handling strategy

Since the Poisson problem does not have a unique solution when BCs are absent, a way to include and process BC information alongside the RHS is required to obtain a model that is able to solve the Poisson problem with arbitrary BCs (as opposed to training different models tailored for one specific set of BCs).

Matrix-based methods such as successive over-relaxation and direct solution handle the BCs by augmenting the RHS vector and FFT methods handle them implicitly by assuming periodic BCs. Conversely, an NN must process boundary information more explicitly by integrating it into the model architecture. Following from John [23] and assuming arbitrary Dirichlet BCs, the proposed methodology involves splitting the original (2D) Poisson problem into one Poisson problem with homogeneous (zero Dirichlet) BCs plus four Laplace problems

where each Laplace problem has three homogeneous BCs plus one non-homogeneous Dirichlet BC identical to one of the BCs in the original problem on the corresponding boundary.

Formally, if we consider the original problem on a rectangular domain D ,

$$\nabla^2 u = f \wedge u([\partial D]_1) = g_1 \wedge u([\partial D]_2) = g_2 \wedge u([\partial D]_3) = g_3 \wedge u([\partial D]_4) = g_4 \quad (2)$$

we can rewrite it in the following form, exploiting the linearity of the Laplace operator

$$\nabla^2(u_h + u_{BC0} + u_{BC1} + u_{BC2} + u_{BC3}) = f \quad (3)$$

such that

$$\nabla^2 u_h = f \wedge u_h(\partial D) = 0 \quad (4)$$

$$\nabla^2 u_{BCk} = 0 \wedge u_{BCk}([\partial D]_j) = \begin{cases} g_k & j = k \\ 0 & j \neq k \end{cases}, j, k \in [0, 1, 2, 3] \quad (5)$$

where $[\partial D]_k$ denotes the k th section of the rectangular boundary.

Thus, it is possible to solve the original problem by first solving the Poisson equation with the original RHS but zero BCs to find u_h , then solving Laplace problems for each BC to find u_{BCk} and sum these results. Similarly, the proposed NN architecture will be composed of two parts – one which solves the homogeneous Poisson problem and another which solves the Laplace problem given one BC.

4 Dataset

The dataset plays a very fundamental role when training NNs, since NNs learn to reproduce the conditional probability distribution of the data $p(\vec{t}|\vec{x})$ as outlined by Bishop [24]. Hence, training on a data subset that does not reflect the probability distribution of the problem that is desired to be solved will give inaccurate results when performing inference on a data subset with a different probability distribution. This is especially important when the model will be trained on synthetic data as with the Poisson equation, since the onus is on the user to ensure the training set reflects the conditional PDF of the ‘real’ data.

Furthermore, the Poisson problem in the most general case will have RHSes and solutions that are finite yet unbounded, which presents a significant obstacle for NNs. Hence, there is a need to normalize the dataset in a way that does not lead to a loss of generality in the predictive performance of the model while constraining the range of the inputs and outputs to a well-defined and consistent interval. Fortunately, the linearity of the Laplace operator allows us to do this by merely scaling the RHS and the solution by some coefficient α :

$$\nabla^2 u = f \implies \alpha \nabla^2 u = \alpha f \quad (6)$$

$$\alpha \nabla^2 u = \nabla^2 \alpha u = \nabla^2 \bar{u} = \alpha f \quad (7)$$

In this work, it was chosen to constrain the RHSes to continuous functions with the range $[-1, 1]$.

Overall, two different methods for dataset generation were developed, one based on a direct solution approach and another on Fourier series. The model will be trained on the data generated by the former, and its performance will be evaluated on data generated by both methods to ensure the model is able to generalize its results to data that extends beyond examples which are generated in a way that is identical to the training set. Furthermore, to avoid overfitting on specific examples, the datasets are generated on-the-go before each batch is fed to the training routine which practically ensures the model never sees an RHS, BC or the corresponding solution twice.

4.0.1 Bicubic-upsampled random arrays

This approach relies on first generating a random RHS and then solving the linear system using a traditional approach. Since the RHS functions were chosen to be continuous, generating grids of random numbers for problems with larger mesh sizes results in extremely noisy RHSes that do not reflect the typical use case of a Poisson solver and are very difficult for NNs to learn from. To rectify this issue, it was instead chosen to generate grids of random numbers with lower resolutions, and then upscale these to the desired grid size using bicubic interpolation as depicted in Figure 1. Owing to the C^2 continuity of bicubic upscaling, this ensures that the resulting RHSes are smooth when the ratio of the final resolution to initial resolution is high enough.

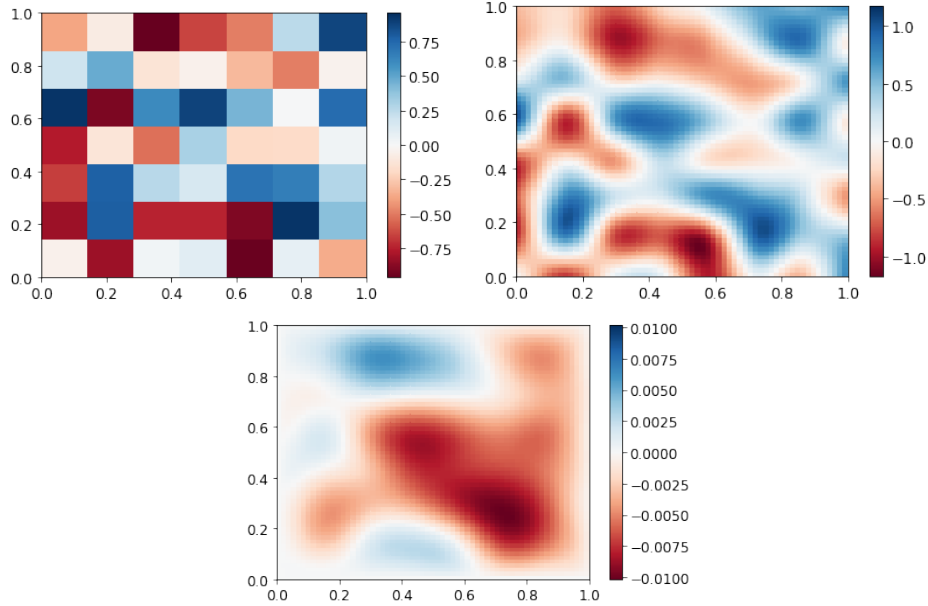


Figure 1: 8×8 low-resolution 2D random number grid (left), the same image upsampled to 64×64 (right) and the solution to the Poisson problem with the upsampled grid as RHS and homogeneous BCs (bottom)

Solutions to the resulting linear systems were computed using the Python algebraic multigrid package PyAMG by Olson and Schroder [25]. Specifically, the ‘classical’ Ruge-Stuben algebraic multigrid method with a tolerance of $1e-10$ was chosen. Calculations were done on a 32-core 64-thread AMD Threadripper 2990WX CPU, using 64 threads. Table 4 in Section 8.5 outlines the wall-clock runtime needed to solve single problems at various grid sizes, excluding the time needed to generate the RHS and BCs. In this work, the coarse grid sizes (across each dimension) were set between 2 and 10.

The significant drawback of this method is the addition of the resolution of the low resolution mesh as a user-defined parameter. Since it is not desired to have the NN learn the mapping from the RHS to the solution for a specific value of this parameter only, this value is randomized for each batch.

4.0.2 Fourier series

For the homogeneous BC case, the Poisson equation has an exact solution in terms of a Fourier series. In an n -dimensional domain, the solution coefficients B_{m_1, \dots, m_n} can be found as follows, with the subscript m_k denoting the m_k th coefficient in the k th direction and L_k denoting the domain length in the k th direction

$$b_{m_1, \dots, m_n} = \frac{2^n}{\prod_k^n L_k} \int_{\Omega} f(x_1, \dots, x_n) \prod_k^n \sin\left(\frac{[m_k + 1]\pi x_k}{L_k}\right) dx_1 \dots dx_n \quad (8)$$

$$B_{m_1, \dots, m_n} = \frac{-b_{m_1, \dots, m_n}}{\sum_k^n \left[\frac{(m_k + 1)\pi}{L_k}\right]^2} \quad (9)$$

It is possible to choose an RHS function f also in the form of a (truncated) Fourier series. If we choose $f = \sum A_{m_1, \dots, m_n} \prod_k^n \sin\left(\frac{[m_k+1]\pi x_k}{L_k}\right)$ Equation 8 reduces to simply

$$b_{m_1, \dots, m_n} = A_{m_1, \dots, m_n} \quad (10)$$

Thus, now any choice of coefficients A can be used to generate a problem-solution pair very efficiently. The choice of coefficients was made at random in the range $[-1, 1]$ and the number of modes in each direction is randomized for each batch, similar to the size of the low resolution mesh in Section 4.0.1. Each coefficient assigned to each mode is then multiplied by $\exp(-\sum_k^n m_k)$ so the modes' magnitudes decay as the wavenumber tends to infinity. This naturally induces a bias in the dataset generated, since the Fourier mode coefficients of not every RHS function will decay exponentially according to the sum of the wavenumbers in each direction. Combined with the fact that this choice for f leads to a loss of generality due to the enforcement of the condition $f(\partial D) = 0$, it was chosen to exclude this method from the training datasets. However, due to the guaranteed machine precision accuracy of the results generated by this methodology, it was retained as a validation and test benchmark to track the performance of the homogeneous BC Poisson equation solver component of the model as shown in Section 8.2.

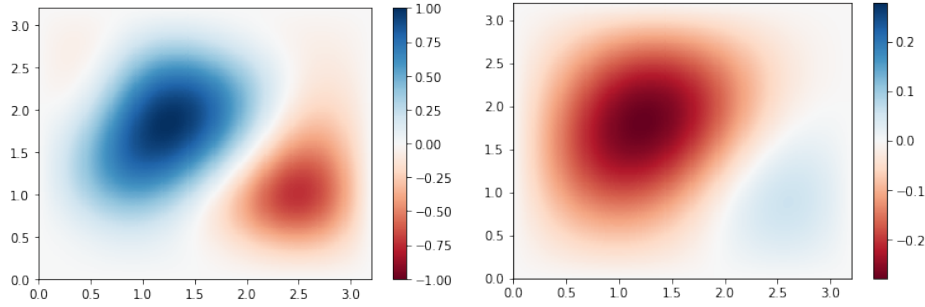


Figure 2: Randomly generated Fourier series-based RHS (left) and the corresponding analytical solution (right) with 4096 modes

5 Neural network architecture

Figure 3 provides an overview of the high-level structure of our architecture. The NN components of the model are the blocks marked as Dirichlet BC NN (DBCNN), which approximates the solution of the Laplace equation with one inhomogeneous Dirichlet boundary, and the Homogeneous Poisson NN (HPNN) which approximates the solution of the Poisson equation with homogeneous BCs.

The architecture mirrors the decomposition in Equations 2 to 5. First, the DBCNN sub-model makes predictions for the four Laplace problems and applies reflection and rotation operations such that the inhomogeneous boundaries align with the corresponding boundary in the original problem. Then, the HPNN model makes a prediction for the Poisson problem with homogeneous BCs. Finally, these results are simply summed to obtain the final prediction for a Poisson problem with four inhomogeneous Dirichlet BCs.

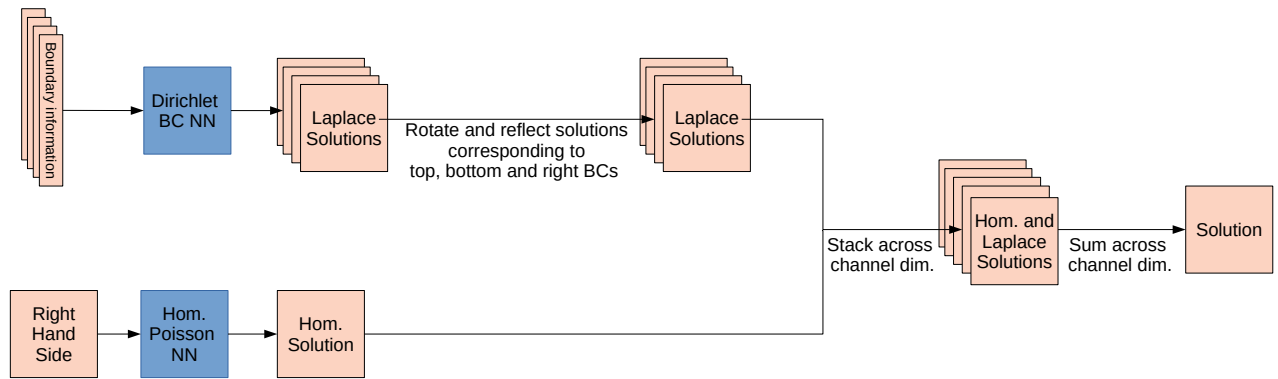


Figure 3: High-level diagram of the Poisson CNN

5.0.1 Homogeneous Poisson NN (HPNN)

The Homogeneous Poisson NN (HPNN) estimates the solution of the Poisson problem with homogeneous BCs and is similar to the Fluidnet architecture by Tompson et al. [20]. Our model expands upon the Fluidnet model by adding ResNet blocks (first proposed by He et al. [26], see Figure 4) after most convolutions, incorporating a substantially larger number of independent pooling operations and merging the results of these operations using an attention mechanism (see Figure 5), and uses dense layers to handle different grid spacings and sizes. Figure 6 summarizes the architecture. The model has two inputs – the RHS and the grid spacing. Figure 6 summarizes the sub-model architecture.

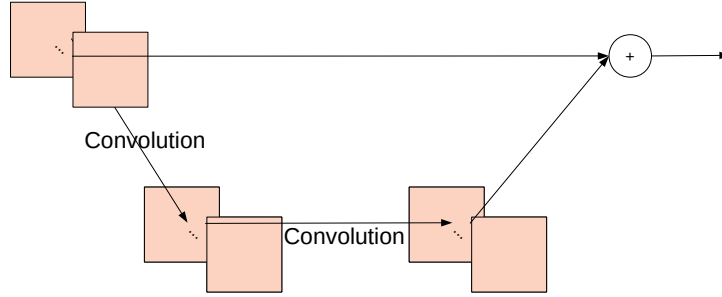


Figure 4: ResNet block diagram

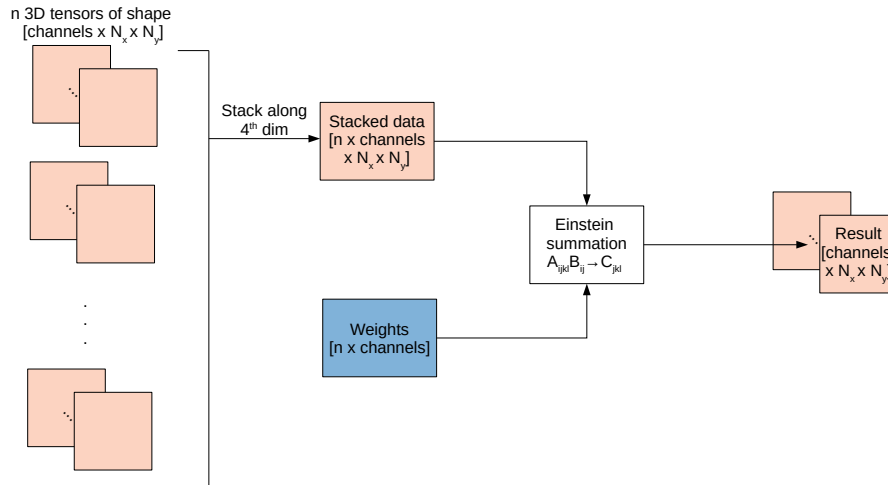


Figure 5: Operation of the attention merge layer

When processing the RHS, first the data is passed through several convolutions. Then, the computation is split into multiple independent pooling operations, each of which applies average pooling of progressively larger pool sizes to capture lower-wavenumber modes and applies further convolutions to the pooled results. Then, the pooled results are upsampled using either bilinear/nearest neighbour upsampling (in the case of the pooling threads with the largest two pool sizes) or transposed convolutions (for threads with smaller pool sizes). Using more traditional upsampling methods for pooling branches with large pool sizes was observed to reduce artefacting in the output; upsampling e.g. a 2×2 input generated using 128×128 pooling from a 200×200 source image requires using a stride² of 128 for the transposed convolution to upsample to the original size, which is excessively large. Finally, the results from all threads are merged using an 'attention merge' layer (see Figure 5) and a few further convolutions are applied.

²Please see Dumoulin and Visin [27] for further details

Meanwhile, the domain information (i.e. Δx , L_x and L_y) is processed by several dense layers, the final one of which has 16 units. The RHS and domain information branches are subsequently merged by multiplying every channel from the RHS branch by one of the outputs of the domain information branch, expressed using tensor notation (without the implicit summation) as

$$A_{ijkl}B_{ij} = C_{ijkl} \quad (11)$$

where index i is the batch dimension, index j is the channel dimension and indices k and l are the spatial dimensions – identical to the channels-first format used in the Tensorflow Keras API for 2D convolutions [28].

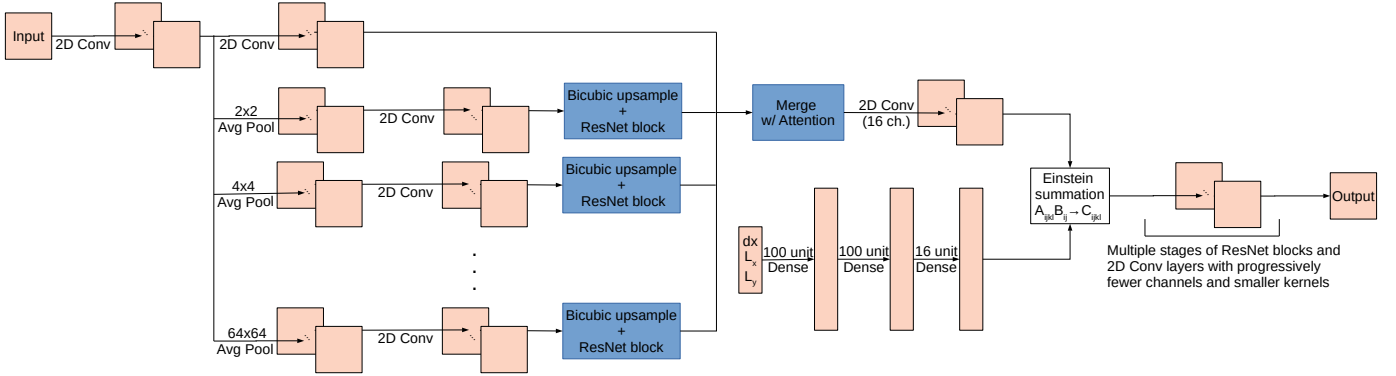


Figure 6: Homogeneous Poisson NN diagram

5.0.2 Dirichlet Boundary Condition NN (DBCNN)

The Dirichlet Boundary Condition NN (DBCNN) estimates the solution of the Laplace equation with one inhomogeneous Dirichlet BC. As inputs, it takes one 1D array containing the BC information plus the grid spacing and the no. of gridpoints in the direction orthogonal to the provided BC. It has two main branches – one which processes the domain and mesh information and another which processes the 1D BC information. Figure 7 summarizes the sub-model architecture.

The branch that processes the BC information first applies a series of 1D convolutions, increasing the number of channels to 256. The array is then reshaped into a 2D array such that the channels outputted by the 1D convolutions become the new dimension (of size 256). Subsequently, a number of 2D convolutions are applied and the resulting array is resampled using bicubic interpolation to have the desired resolution in the new dimension.

Domain information branch, meanwhile, processes the values of Δx and the size of the domain in both directions via a number of dense layers, the final dense layer having 4096 units. The result of the final dense layer is then reshaped into a 32×128 2D array and a number of convolutions along multiple pooled branches similar to the HPNN are performed. Then, bicubic upsampling is applied to match the desired grid size and the result is merged with the BC information branch. Several further convolutions are applied before the final result is produced.

It should be noted that this model returns results such that the prescribed BC is always on the left vertical boundary of the domain. However, a series of rotations and reflections are sufficient to modify the result such that any other boundary is the nonzero boundary instead.

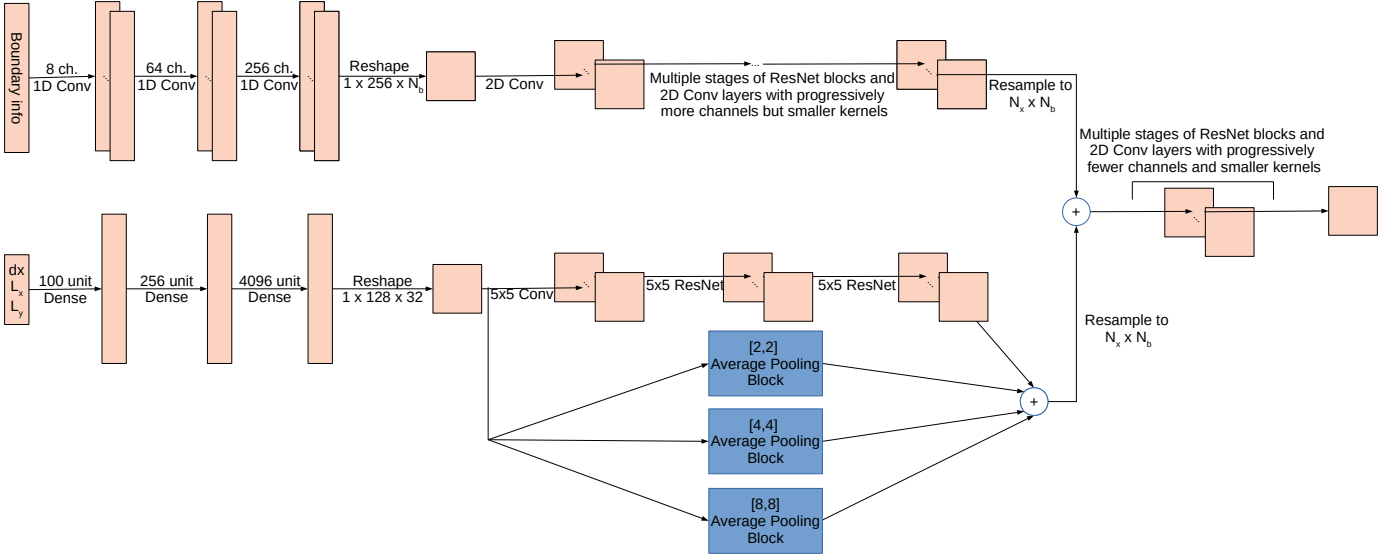


Figure 7: Dirichlet Boundary Condition NN diagram

6 Loss function and Approximation of Loss Value

In typical machine learning applications, it is common to use the mean squared error (MSE) defined in Equation 21 as the loss function. However, as shown in multiple studies on image-to-image translation using convolutional models such as those by Isola et al. [19], MSE loss does not typically lead to good results. As an alternative, since the targets are strictly smooth functions, the continuous version of the L^p norm between the output and the target

$$\left[\frac{1}{A} \int_A (y - t)^p dA \right]^{1/p} \quad (12)$$

presents a more meaningful loss for a pair of continuous functions, where y is the prediction, t is the target and A is a finite region of \mathbb{R}^n .

One problem is that we know the functions' values only on the gridpoints of a rectangular grid within the domain. In a naive approach, we could evaluate the expression in Equation 12 by using a polynomial reconstruction method (in fact, MSE loss can be interpreted as doing this with the midpoint rule) and integrating the piecewise polynomial. A more accurate alternative is Gauss-Legendre quadrature. Though having a theoretical background in approximating the integrand from a finite number of samples using Legendre polynomials (samples being taken from the root locations of the Legendre polynomials), in practice, this methodology can be written down for a function $h : \mathbb{R}^n \rightarrow \mathbb{R}$ as

$$\int_V h(x_1, x_2, \dots, x_n) dx_1 \dots dx_n \approx \sum_{i_1=1}^{k_1} \dots \sum_{i_n=1}^{k_n} \left(\prod_{j=1}^n w_{i_j} \right) h(\bar{x}_{1i_1}, \dots, \bar{x}_{ni_n}) \quad (13)$$

where k_l is the order of the quadrature in the l th direction, \bar{x}_{li_l} is the i_l th quadrature point (i.e. Legendre polynomial root) in the l th direction and w is a vector containing the quadrature weights (hence w_{i_j} denotes the i_j th weight in the j th direction). Applying this formula to Equation 12 for $y, t : \mathbb{R}^2 \rightarrow \mathbb{R}$ with k weights in

both directions, we can write

$$\left[\frac{1}{A} \int_A (y(x_1, x_2) - t(x_1, x_2))^p dA \right]^{1/p} \approx \left[\frac{1}{A} \sum_i^k \sum_j^k w_i w_j [y(\bar{x}_{1_i}, \bar{x}_{2_j}) - t(\bar{x}_{1_i}, \bar{x}_{2_j})]^p \right]^{1/p} \quad (14)$$

This approach, however, relies on knowing the values of y and t at the quadrature points \bar{x}_1, \bar{x}_2 which are not equispaced and therefore cannot be made to coincide with the grid points using a simple affine transformation.

To overcome this issue, $y(\bar{x}_1, \bar{x}_2)$ and $t(\bar{x}_1, \bar{x}_2)$ were approximated using bilinear interpolation within the ‘cell’ enclosing each quadrature point. In practice, for each quadrature point, the value is a linear combination of the 4 known values on the corners

$$y(\bar{x}_1, \bar{x}_2) \approx [b_{00} \quad b_{01} \quad b_{10} \quad b_{11}] \begin{bmatrix} y_{i,j} \\ y_{i+1,j} \\ y_{i,j+1} \\ y_{i+1,j+1} \end{bmatrix} = \vec{b}^\top \vec{y} \quad (15)$$

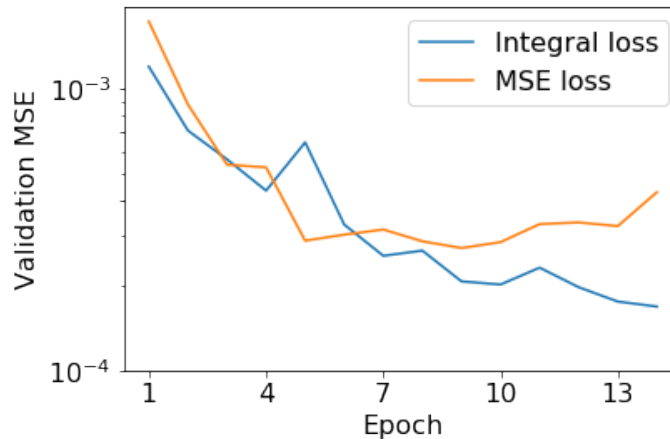
where the weight vector \vec{b} depends on the coordinates of the quadrature point and the gridpoints. Denoting \vec{y}_{ij} as the vector containing the values of the variable in question for the i th quadrature point in the x_1 direction and the j th quadrature point in the x_2 direction, we can rewrite Equation 14 as

$$\left[\frac{1}{A} \int_A (y(x_1, x_2) - t(x_1, x_2))^p dA \right]^{1/p} \approx \left[\frac{1}{A} \sum_i^k \sum_j^k w_i w_j [\vec{b}_{ij}^\top (\vec{y}_{ij} - \vec{t}_{ij})]^p \right]^{1/p} \quad (16)$$

During training, it was found that augmenting the integration with a mean absolute error (MAE) loss component sped up the loss minimization. Hence, the final expression for the loss is

$$L = \left[\frac{1}{A} \sum_i^k \sum_j^k w_i w_j [\vec{b}_{ij}^\top (\vec{y}_{ij} - \vec{t}_{ij})]^p \right]^{1/p} + \frac{\lambda}{N} \sum_i^N |y_i - t_i| \quad (17)$$

Experimentation during training indicated that values of $\lambda = 1.0$ and $p = 2$ provide good performance. Figure 8 juxtaposes the performance of two otherwise identical Dirichlet BC NN models, one of which has been trained with MSE loss and the other with the Integral loss on grid sizes between 64 and 85 in each direction and Δx values on the interval $[0.005, 0.05]$ over 15 epochs of 50 batches of 20 example problems each for a total of 15000 examples. The integral loss demonstrates substantially smoother results.



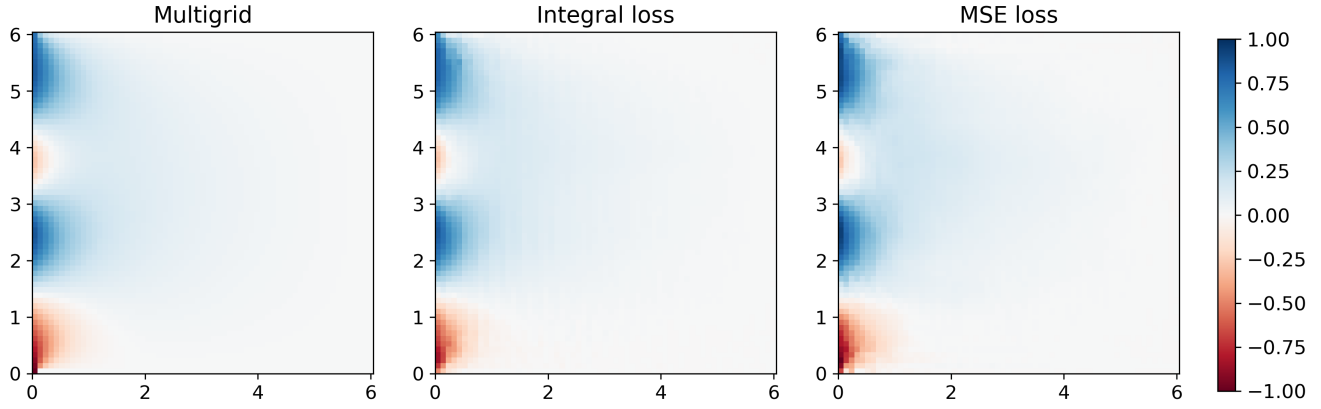


Figure 8: Validation MSE-epoch plot (top), sample direct solution to a randomly generated Laplace problem (bottom left) and Dirichlet BC NN predictions with models trained with integral (bottom middle) and MSE (bottom right) losses

7 Training

The model was implemented using Tensorflow Keras 2.0 Beta. The sub-models were trained independently; no further training was carried out for the full model configuration shown in Figure 3. Adam was chosen as the optimizer method, with an initial learning rate of 10^{-4} for all models. Learning rate was dynamically tapered as MSE plateaued. To determine the when to stop the training, the Tensorflow Keras early stopping callback [29] based on the mean squared error with 20-epoch patience was used. Table 1 summarizes the information regarding the number of samples used to train each model.

Model	Batch size	Batches per epoch	Epochs	Samples
HPNN	10	50	86	43000
DBCNN	10		92	46000

Table 1: Details of the number of samples used to train each sub-model

Furthermore, a number of best practice guidelines for both training and tweaking the model architecture were established for ensuring the best model performance:

- Including the full domain information as an input (L_x and L_y in addition to Δx) is important since otherwise convolutional models will not receive information regarding the domain size.
- Final layers should have small kernels to prevent artefacting near the domain edges, while initial layers should have large kernels to capture larger-scale information.
- Adding as many pooling levels as possible is crucial to allow the model to capture information at multiple scales.
- Deconvolutional upsampling provides superior results when reversing pooling operations with small pool sizes, while bilinear/nearest neighbour are better for very large pool sizes (e.g. 64×64)
- L2 regularization is important to prevent overfitting
- Leaky ReLUs are superior to regular ReLUs in the intermediate layers for this task (cf. Dying ReLU problem)
- Residual connections massively boost performance

8 Results and performance

In this section we show the performance of a Poisson CNN model, the submodels of which were trained independently on problems with meshes containing 192 to 228 gridpoints in each direction and Δx values between 0.005 and 0.05. Starting from random problems generated in a manner similar to the training set, we subsequently demonstrate the generalization performance of the model on two analytical examples. Finally, we evaluate the performance of the model when used on grids outside the training range and compare the wall-clock runtime of the model to the multigrid algorithm.

Table 2 outlines the number of parameters for the models with the specific choice of hyperparameters (e.g. kernel sizes, no. of channels) made. It should be noted that our choice does not represent a necessarily optimal choice for these hyperparameters, as this work is meant as a feasibility study.

	HPNN	DBCNN	Poisson CNN
# of parameters	6529998	2214561	8744559

Table 2: Summary of the total number of parameters

Table 3 gives an overview of the performance of the model in terms of the MAE, mean absolute percentage error (MAPE) and the percentage of gridpoints in each case for which the model made a prediction within 10% of the target for the selected test cases as well as averaged results for larger sets of similar examples where applicable. Sections 8.1 to 8.3 outline the test cases chosen and give greater detail regarding the performance of the model in each test case.

Case	MAE	MAPE (%)	% of gridpts within 10% of target	
HPNN (Fig. 9)	2.31×10^{-3}	16.87	53.11	
HPNN – 600 example avg.	1.26×10^{-2}	16.88	56.02	
Examples similar to the training set (Section 8.1)	DBCNN (Fig. 10)	1.66×10^{-2}	27.73	18.49
	DBCNN – constant BC (Fig. 11)	1.19×10^{-2}	8.78	75.60
	DBCNN – 600 example avg.	1.93×10^{-2}	30.61	20.03
	Full model (Fig. 13)	3.28×10^{-2}	18.75	38.62
	Full model – 600 example avg.	4.29×10^{-2}	21.49	33.78
Rand. Fourier coeffs. (Section 8.2)	HPNN (Fig. 14)	7.47×10^{-3}	12.47	51.56
	HPNN – 600 example avg.	1.16×10^{-2}	15.31	43.53
Taylor-Green Vortex (Section 8.3)	HPNN (Fig. 16)	2.08×10^{-2}	15.57	55.63
	DBCNN (Fig. 17)	8.01×10^{-3}	24.31	24.03
	Full model (Fig. 18)	2.50×10^{-2}	17.06	39.54

Table 3: Summary of the results presented in this section, plus averaged figures for larger numbers of examples for each case where applicable. Note that gridpoints with absolute percentage errors above 200% were excluded from the MAPE calculation due to MAPE values approaching infinity near the zero solution contours.

8.1 Examples similar to the training set

One of the most basic yet crucial tests for any ML algorithm is the ability to make correct predictions on previously unseen data that comes from a dataset that has the same conditional probability distribution between the inputs and outputs. In typical machine learning applications, this testing is done by splitting the dataset (of e.g. photos) into a training and a validation set and observing if a model that performs well on the training set does equally well on the validation set. In our approach, since each batch of training data is generated from random noise synthetically just before being fed to the training loop, the most basic test instead involves observing model performance on examples generated in the same way as the training data. This section presents examples generated in the same manner as the training data first for each submodel individually, and finally presenting an example for a Poisson problem with four non-homogeneous Dirichlet BCs.

8.1.1 Homogeneous Poisson NN

Figure 9 depicts the performance of the Homogeneous Poisson NN on a random example generated in the same manner as the training data. The model displays good predictive accuracy, with the majority of the predictions lying within 10% of the target. A substantial proportion of the predictions that lie outside this 10% band are clustered around the contours where the solution $u = 0$ which leads to high percentage errors around these contours despite good predictions in terms of the numerical value.

The most notable inaccuracies (in terms of the absolute values) lie near points where the ground truth (multigrid solution) has a local maximum or minimum due to slight mispredictions of both the location and the value of these local extrema, in addition to oscillatory behaviour near the edges which cause nonzero predictions originating from the necessity to zero-pad the edges of the inputs to retain the grid shape. It was observed that large kernel sizes amplify the severity of these oscillations near the edges, which necessitate the use of small kernels in the final layers of the CNN even though large kernel sizes especially in the initial layers are helpful to capture larger scale structures in the problem.

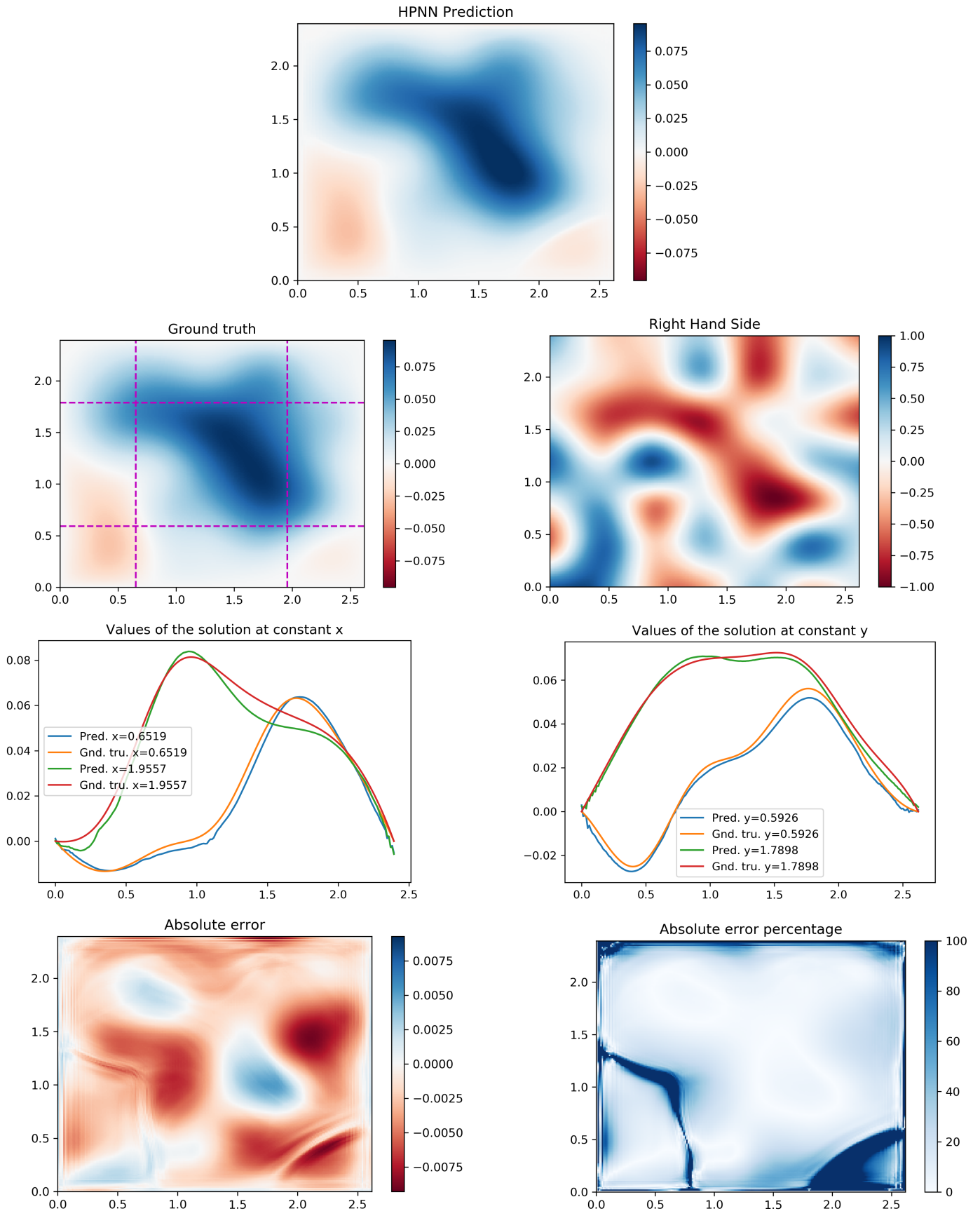


Figure 9: Performance of the Homogeneous Poisson NN model on an example with grid size 221×202 and $\Delta x = 1.19 \times 10^{-2}$. Purple dashed lines on the ground truth image (2nd row, left) depict the spatial positions of the constant x and y lines used to generate the images in the third row.

8.1.2 Dirichlet BC NN

As shown in Figure 10, the Dirichlet BC NN reproduces the multigrid solution with a good degree of accuracy in terms of the MAE. The largest absolute errors occur due to the oscillatory behaviour near the left boundary, caused by the padding issues explained in Section 8.1.1 being magnified by the large solution magnitudes in this region.

The performance in terms of the percentage of gridpoints with predictions within 10% of the target is worse than the HPNN sub-model, though this figure must be viewed in light of the observation from the error map that the percentage errors increase progressively as we move in the positive horizontal direction. Though the percentage errors rise as we approach the right boundary, the hyperbolic sine-shaped solution profile in this direction ensures the absolute values at these points are c. 3 orders of magnitude smaller than near the left boundary – hence the absolute error remains very small. Considering the chosen loss function depends only on the absolute errors, this translates to very small gradients for the errors in this part of the domain. Augmenting the loss with a scale-invariant function such as MAPE was tried to combat this issue, but led to substantially worse accuracy in terms of both MAE and MAPE.

It should also be noted that the performance of the DBCNN is dependent on the 'complexity' of the chosen BC. Figure 11 illustrates this with the simplest possible BC – a constant value on the left boundary. For a simple case like this the model achieves very accurate predictions, with predictions at over three quarters of the gridpoints within 10% of the target and MAPE below 10% despite never seeing a constant BC during training.

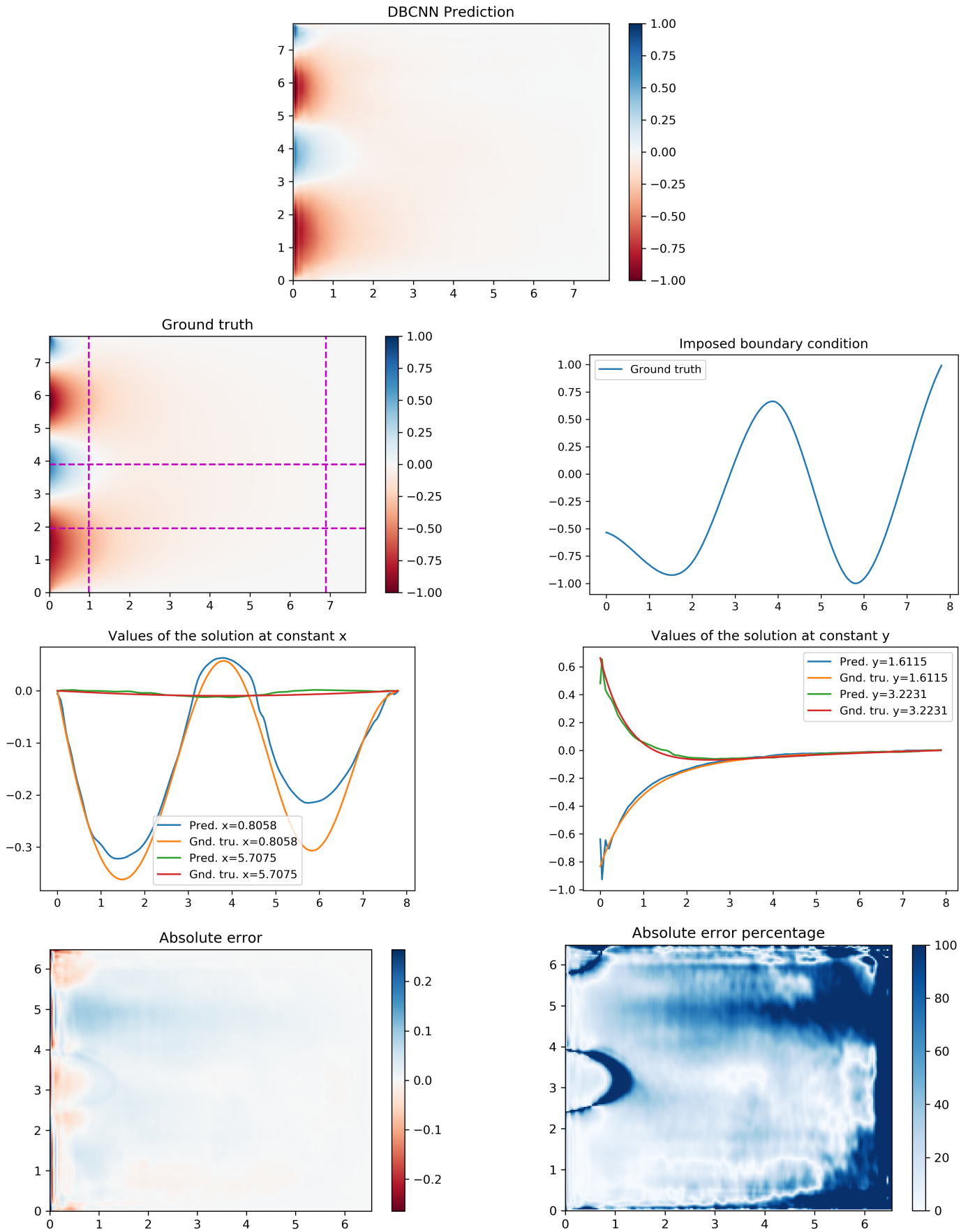


Figure 10: Performance of the DBCNN model on an example generated in the same manner as its training data, with a grid size of 195×193 and $\Delta x = 3.36 \times 10^{-2}$. Purple dashed lines on the ground truth image (2nd row, left) depict the spatial positions of the constant x and y lines used to generate the images in the third row.

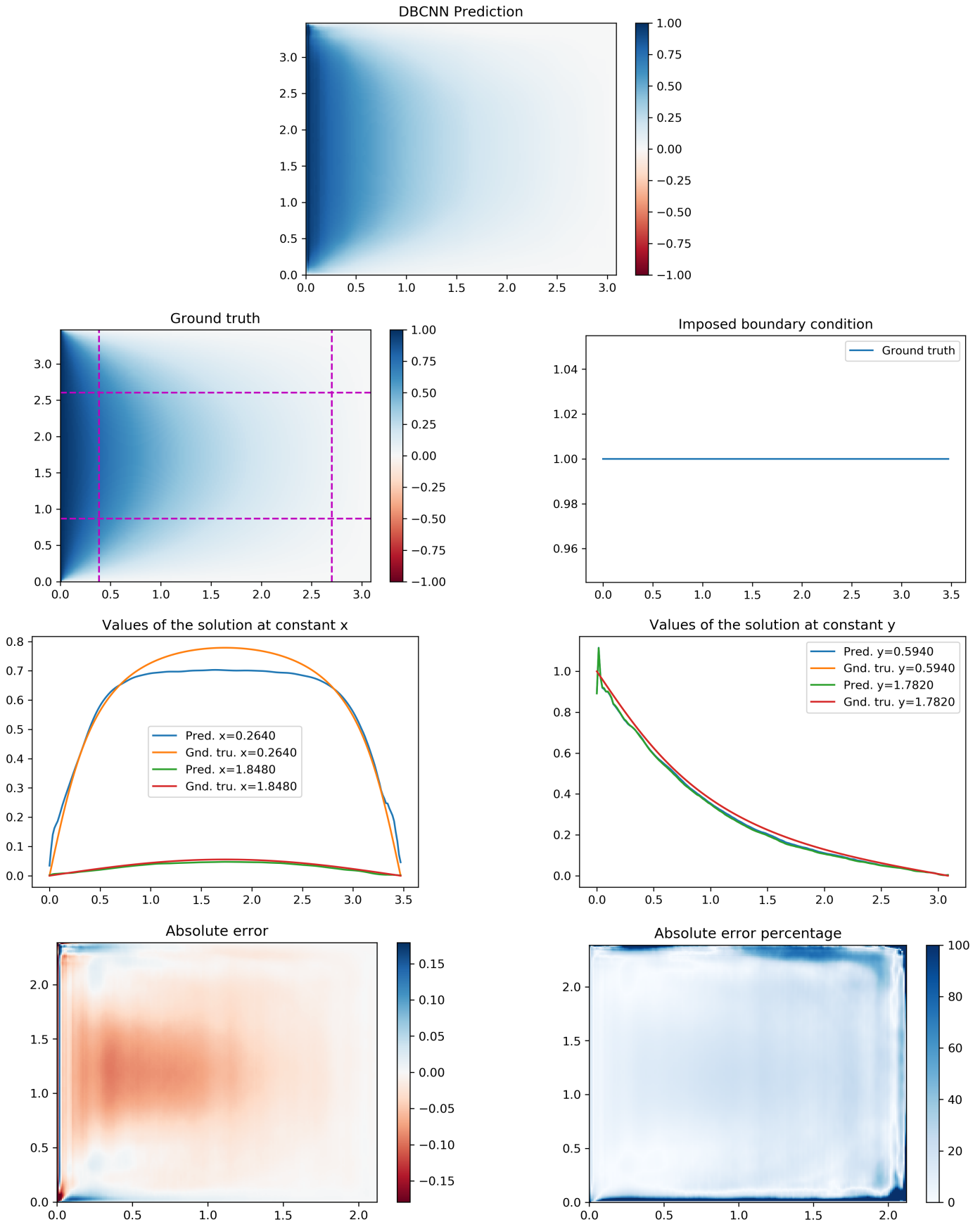


Figure 11: Performance of the Dirichlet BC NN model on an example generated in the same manner as its training data, with a grid size of 193×217 and $\Delta x = 1.10 \times 10^{-2}$ Purple dashed lines on the gnd. tru. image (2nd row, left) depict the spatial positions of the const. x and y lines used to generate the images in the third row.

8.1.3 Poisson CNN (Full model)

Figure 13 depicts the performance of the full model on the Poisson problem in Figure 12. The performance of the model in terms of MAPE lies just above that of the HPNN submodel, though the MAE exceeds that of both sub-models due to larger peak solution magnitude achieved. The level of accuracy achieved is particularly noteworthy since it was achieved despite the substantially more complicated BCs imposed, demonstrated above to be detrimental to the accuracy of the DBCNN sub-model.

As demonstrated by these results, the Poisson CNN architecture proposed is capable of providing good estimates for Poisson problems with four inhomogeneous BCs when given RHS function – BC combinations that are previously unencountered on meshes which have grid spacings and grid sizes that fall within the values seen during training.

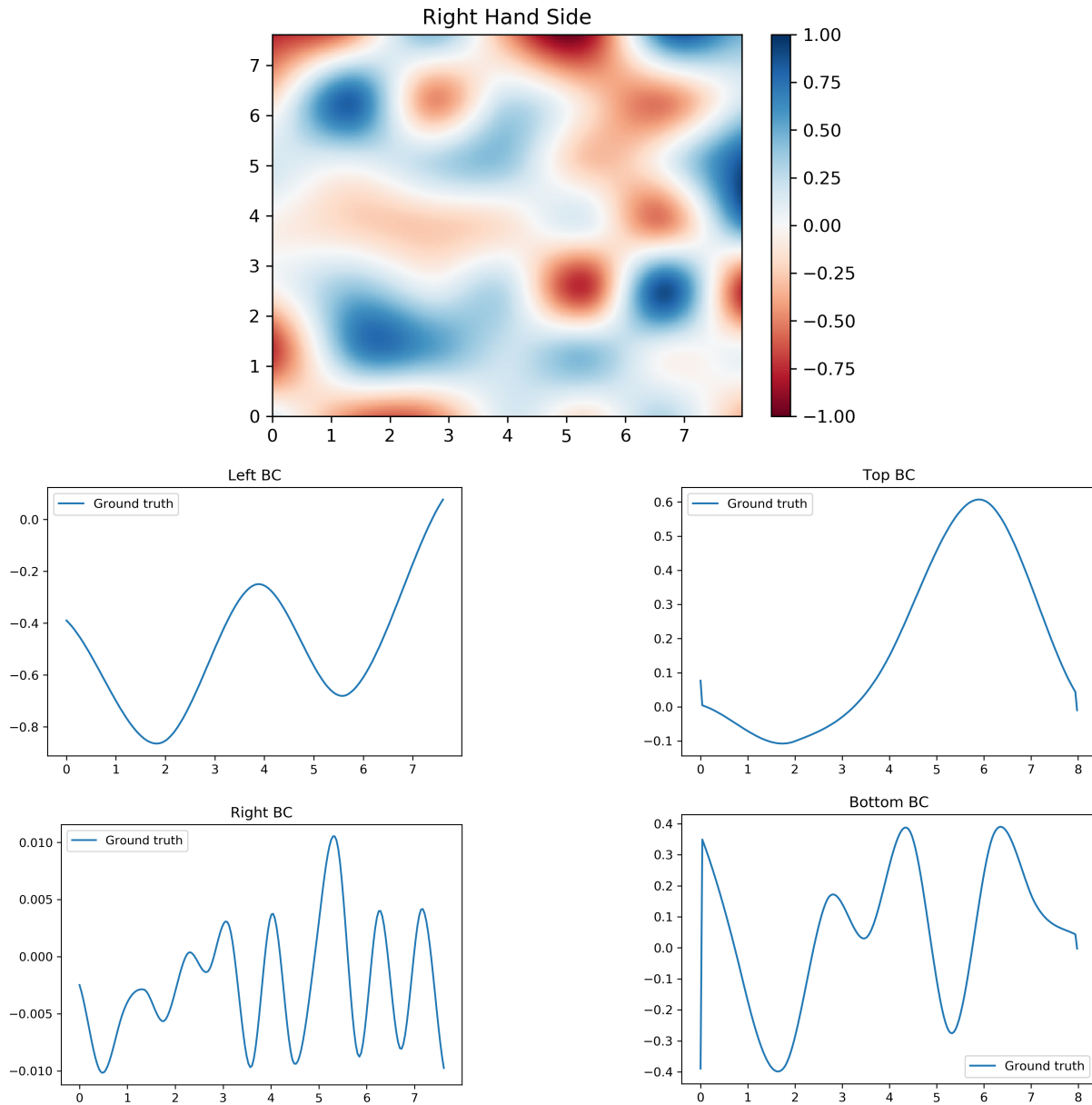


Figure 12: RHS function (top) and the BCs (bottom rows) used to generate Figure 13

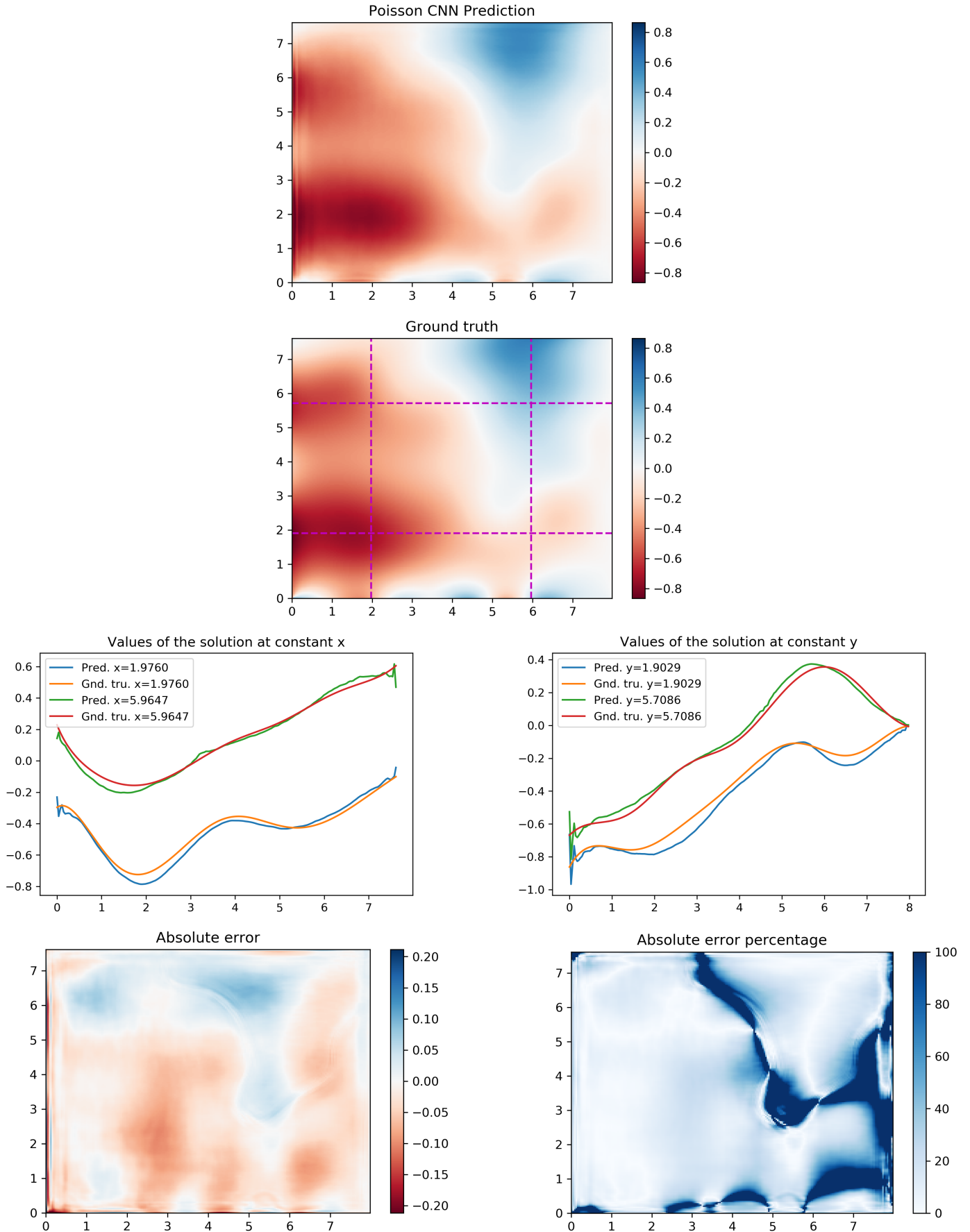


Figure 13: Performance of the Poisson CNN model on an example generated in the same manner as its training data, with a grid size of 218×208 and $\Delta x = 3.66 \times 10^{-2}$. Purple dashed lines on the gnd. tru. image (2nd row) depict the spatial positions of the const. x and y lines used to generate the images in the third row.

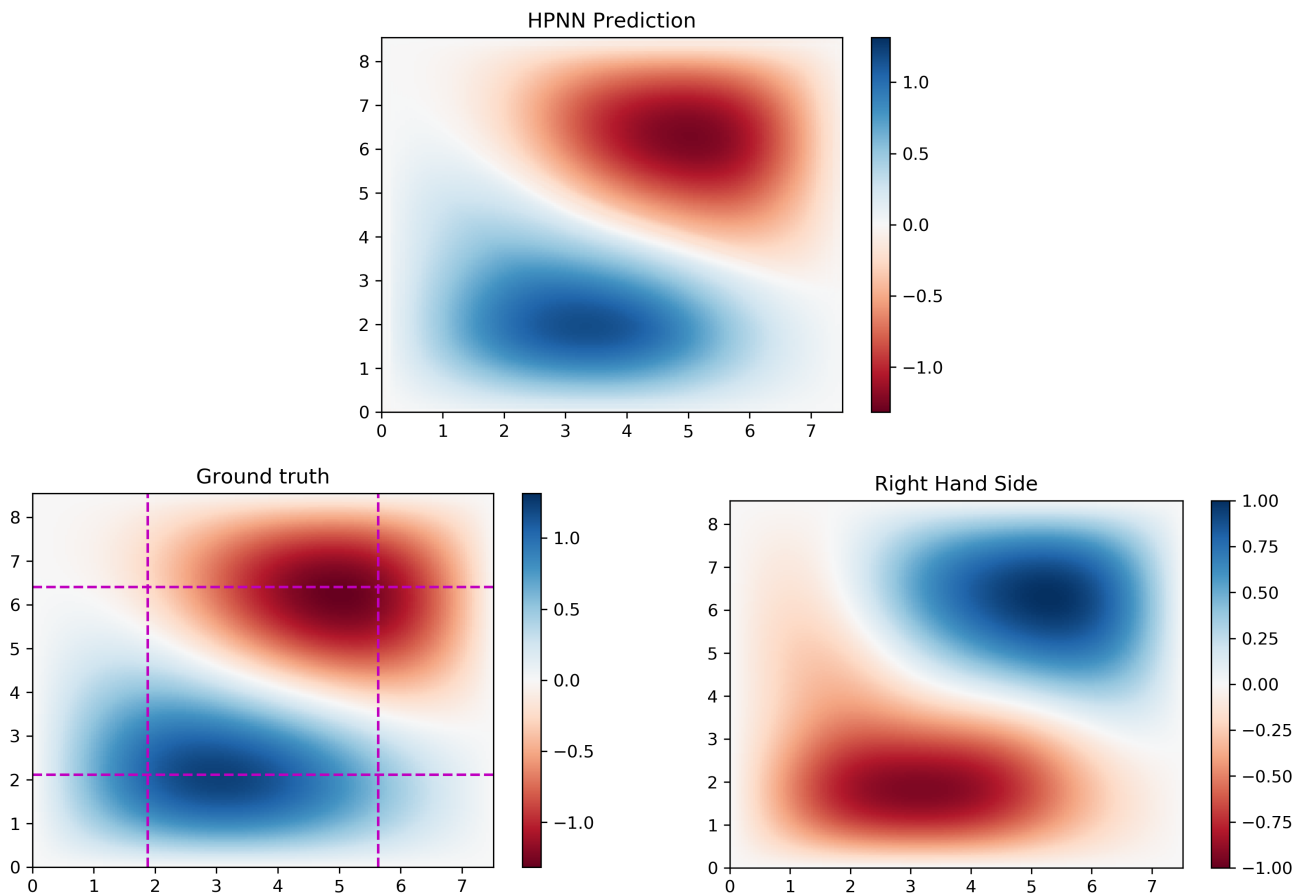
8.2 Random Fourier coefficients

The results presented in Section 8.1 rely on a dataset with its own tunable 'parameters' such as the size of the low-resolution grid as explained in Section 4.0.1 and the tolerance set for the multigrid solver. Hence, benchmarking the performance of the model on data generated in a different way is important to assess the generalization performance since it allows us to determine whether the model truly learned to estimate the solution of the Poisson equation or overfitted to reproduce the statistics of the training dataset.

As explained in Section 4.0.2, using Fourier series with random coefficients presents a method to generate random problems that can be solved analytically, though with the drawback of generating results with only homogeneous BCs. Hence, only the performance of the HPNN sub-model is benchmarked.

8.2.1 Homogeneous Poisson NN

Figure 14 displays the performance of the HPNN model on an example with an RHS composed of random Fourier coefficients. The Homogeneous Poisson NN model shows very good predictive accuracy for this test case. Both MAE and MAPE are lower than what the model achieved on examples similar to the training set, though there is a slight regression in terms of the proportion of the predictions within 10% of the target when considering a large number of examples. Areas with the largest errors are identical to the previous dataset – vicinity of local extrema.



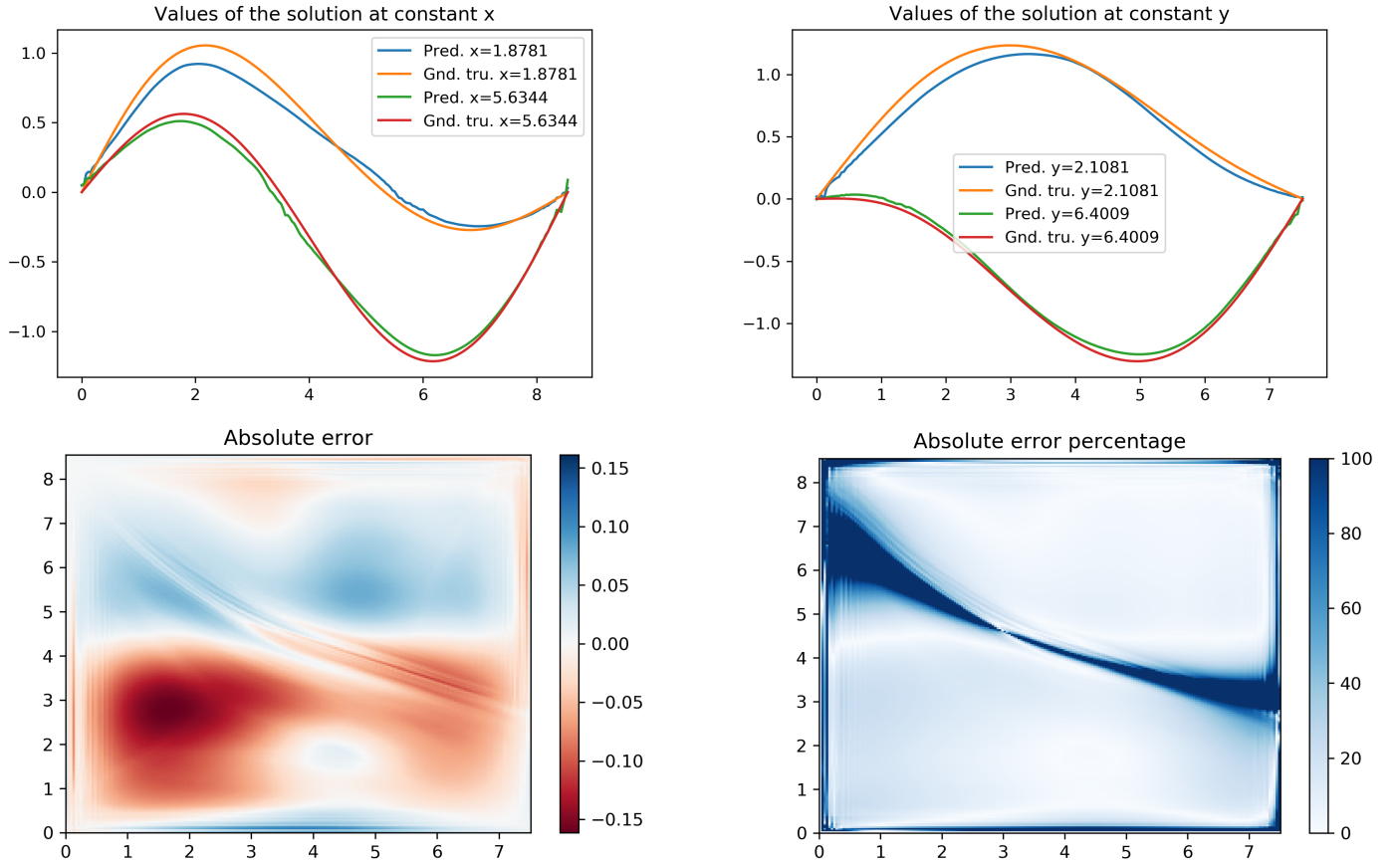


Figure 14: Performance of the Homogeneous Poisson NN submodel on an RHS function with a total of 4096 random Fourier coefficients, with a grid size of 196×223 and $\Delta x = 3.83 \times 10^{-2}$ Purple dashed lines on the ground truth image (2nd row, left) depict the spatial positions of the constant x and y lines used to generate the images in the second row.

8.3 Taylor-Green Vortex (TGV) Pressure Field

Using the pressure field of the Taylor-Green vortex (TGV), such that the time-dependent term and density are set as unity for simplicity, presents an easy-to-construct analytical test case. We can construct a Poisson problem in the domain $[0, 2\pi] \times [0, 2\pi]$ by setting the solution u as the TGV pressure field as follows

$$u = -\frac{1}{4}(\cos(2x) + \cos(2y)) \quad (18)$$

$$\therefore \text{RHS} = \nabla^2 u = \cos(2x) + \cos(2y) \quad (19)$$

with the BC

$$b(t) = -(\cos(2t) + 1)/4 \quad (20)$$

along each boundary, where t is the coordinate along the boundary. Figure 15 pictorially depicts the functions in Equations 19 and 20. As a benchmark case, we investigate the performance of the model on this problem with the largest mesh the model has seen during training – 228×228

Figures 16, 17 and 18 show the performance of the HPNN, DBCNN and Poisson CNN models respectively.

The HPNN sub-model performed at a level in line with the results displayed in Sections 8.1.1 and 8.2 when predicting on the RHS function. The model achieved predictions within 10% of the target at over half of the gridpoints and reproducing key solution features such as symmetry about the $x = y$ line. Mirroring the

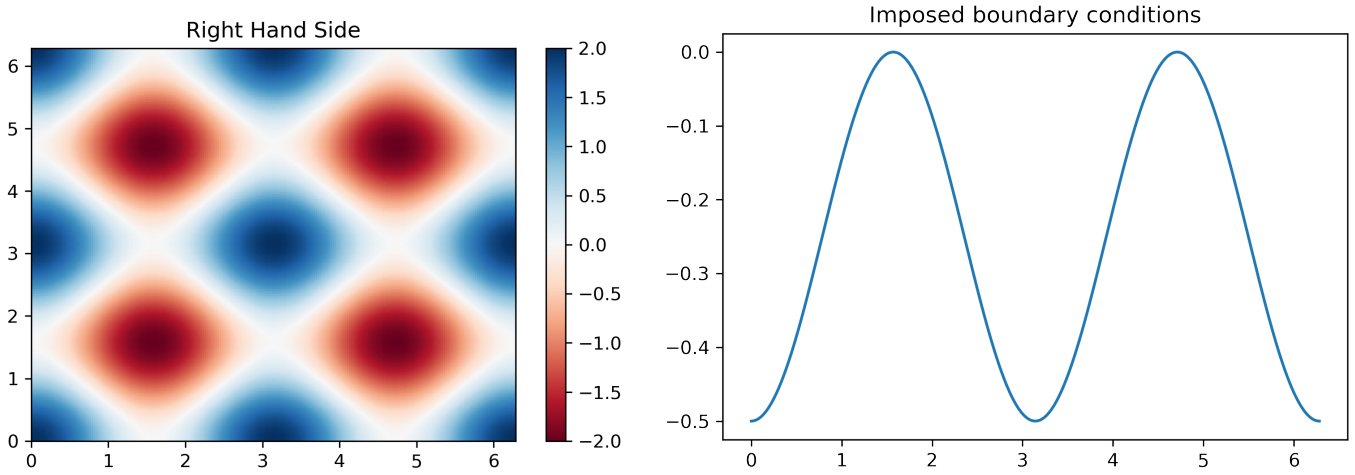


Figure 15: RHS function (left) and the BC imposed on all edges (right) in the TGV test case

previous cases, largest errors are concentrated near local extrema, particularly near the local minimum in the middle of the domain.

The DBCNN sub-model performed slightly better in this case than compared to the 600-sample average shown in Table 3. Though providing somewhat grainy results and underpredicting the peak magnitude of the solution along the $y = (2k + 1)\pi/2$ contours where the BC value approaches 0, the predictions along the mid-section of the domain are excellent.

Considering the good performance of the two sub-models on their respective sub-problems, the full Poisson CNN model expectedly performs well on the complete problem with four boundary conditions. The MAPE of the full model lies between that of the two sub-models and is also slightly lower than the previous 600-sample average shown in Table 3. Important solution features such as the sharp zero solution contours along the $x + y = (2k + 1)\pi/2$ lines are replicated.

Overall, all models demonstrate strong performance in this analytical test case, giving further evidence that the model did not overfit on the training data.

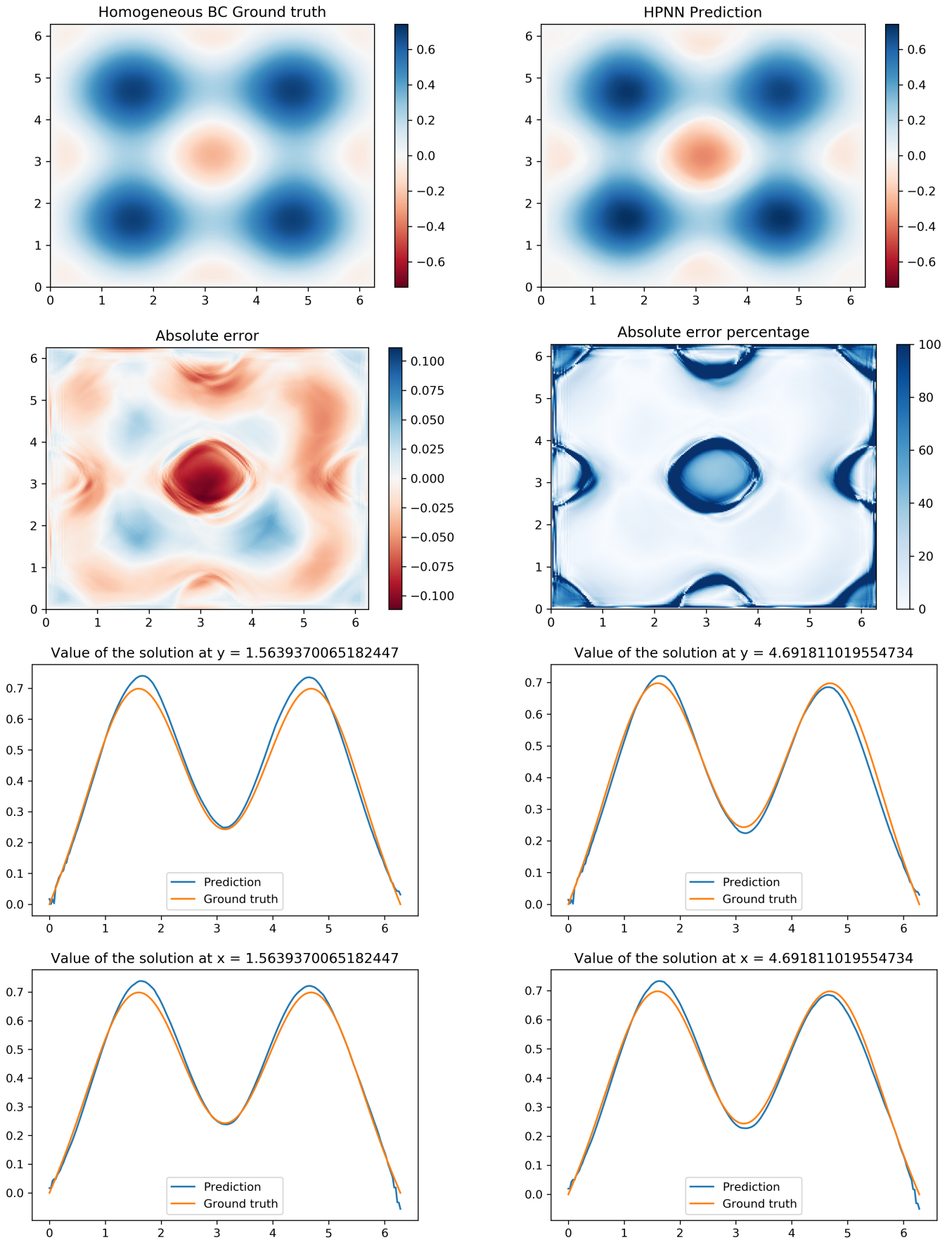


Figure 16: Prediction of the HPNN sub-model on the TGV case.

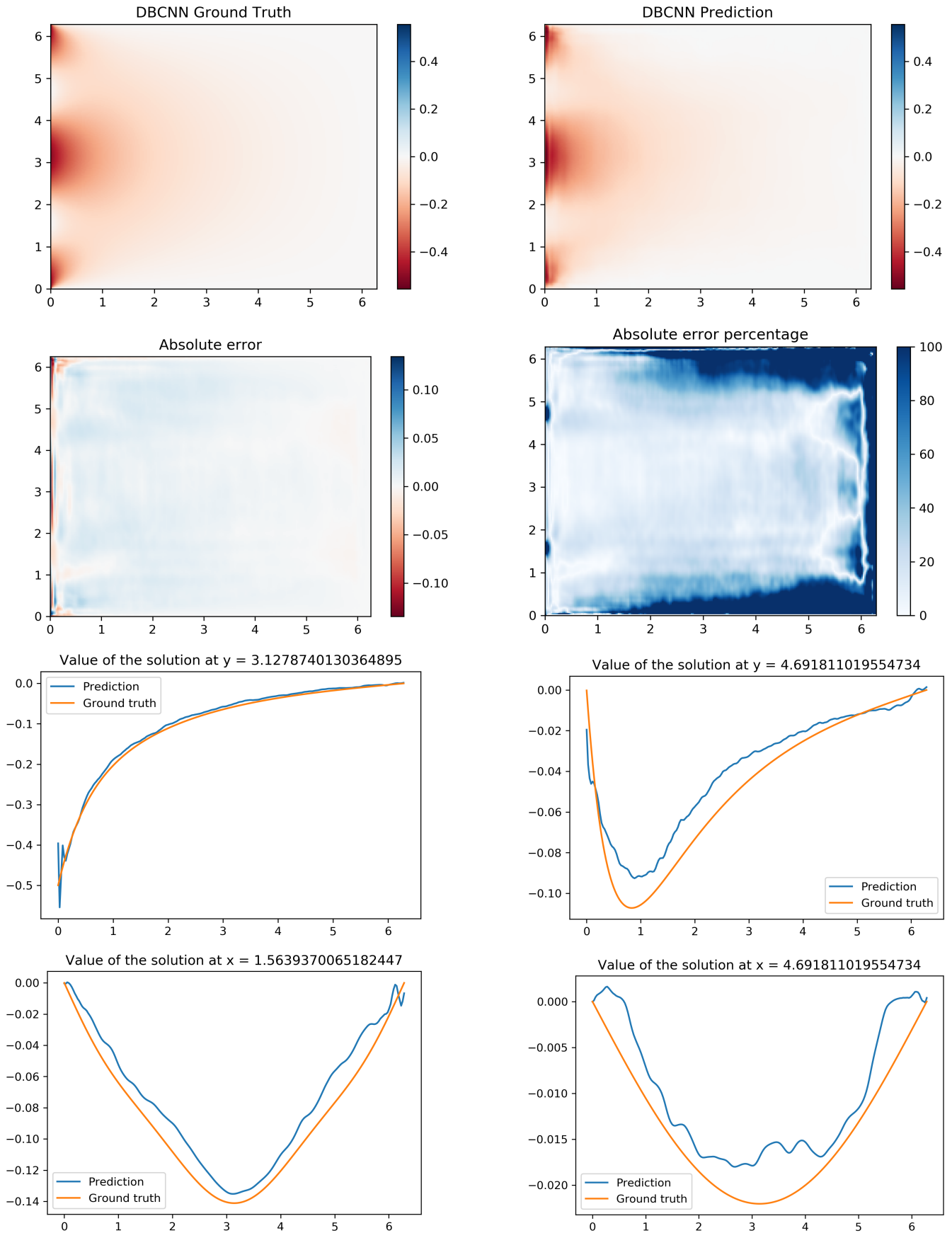


Figure 17: Prediction of the DBCNN sub-model on the TGV case

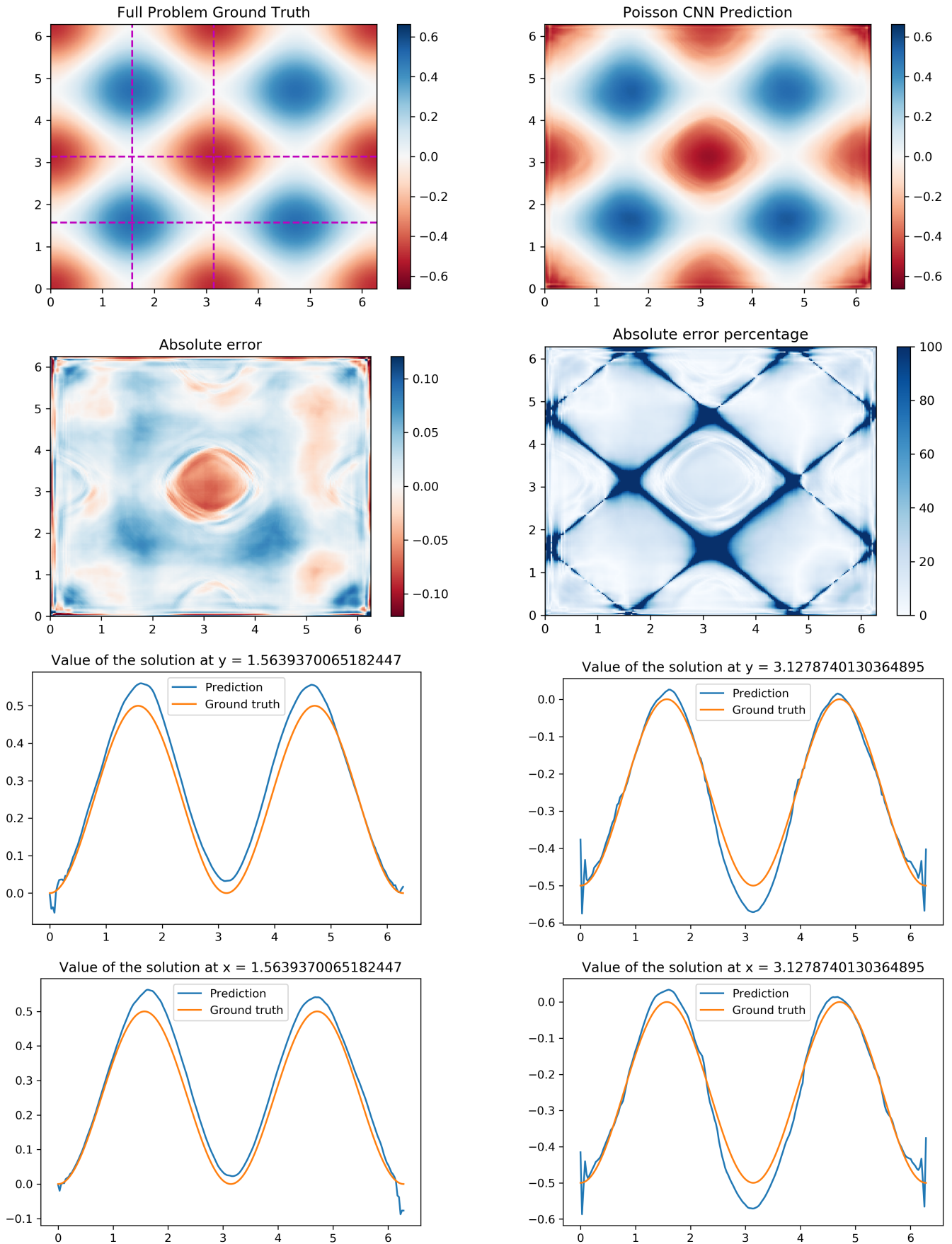


Figure 18: Prediction of the full model on the TGV case

8.4 Performance with previously unseen grid parameters

An important aspect of the generalization performance of the model is whether it is able to handle meshes with parameters such as grid spacing and sizes outside the range encountered during training. Figure 19 shows the RMS error of the model prediction relative to the analytical solution on the same Taylor-Green Vortex case shown in Section 8.3 with progressively denser grids.

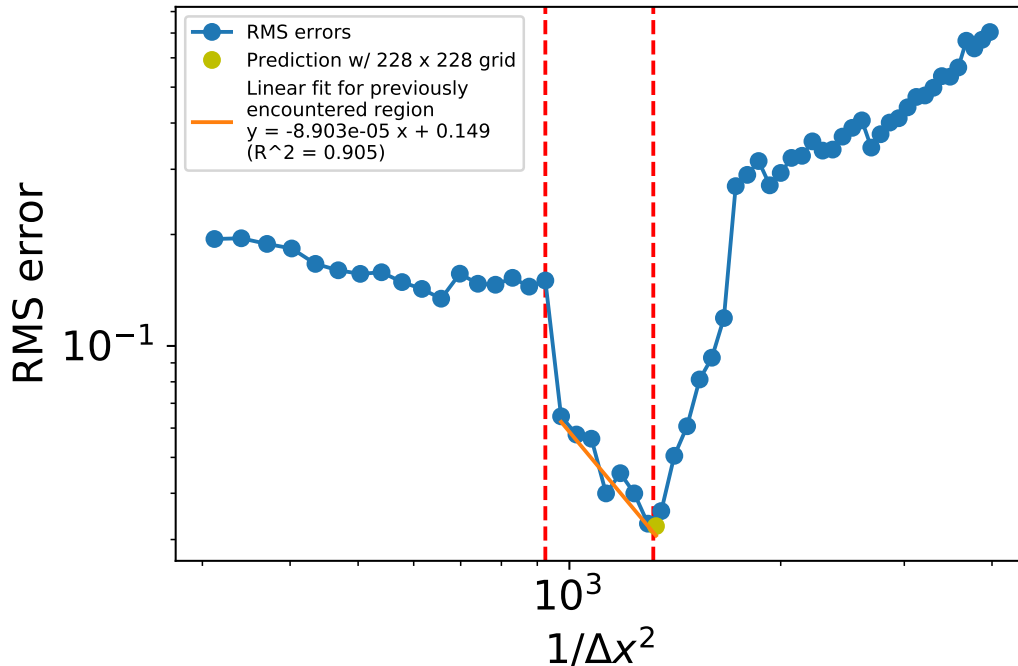


Figure 19: RMS error model output w.r.t. the analytical solution versus mesh density for the TGV case. Interval of mesh sizes encountered in training is marked by red lines. Yellow dot indicates the results presented in Section 8.3

The results clearly indicate that the model is incapable of handling meshes that lie outside the range of the training data. Unlike a traditional numerical algorithm, where we would expect a linear decrease of the RMS error with a slope equal to the order of the method, the NN model achieves the same only within the range of encountered meshes and gives inaccurate results outside this region. Figure 20 depicts predictions at three mesh sizes outside the training range.

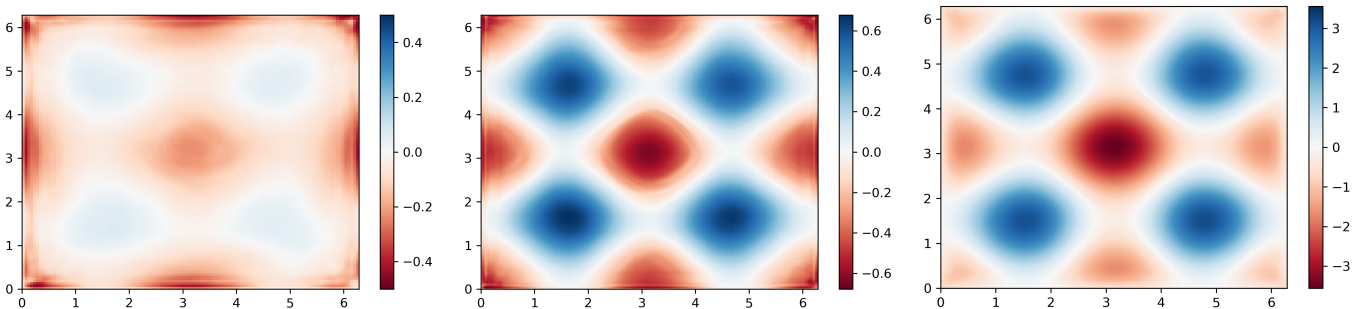


Figure 20: Poisson CNN predictions on 120×120 (left), 240×240 (middle) and 500×500 (right) grids for the TGV case

In the 120×120 case, the model gives an answer completely dissimilar to the analytical solution, however, the mesh sizes which exceed the training range retain general solution features which are reminiscent of the analytical solution though with the wrong scale. The RMS error is higher for previously unseen higher-resolution

meshes compared to previously unseen lower-resolution meshes despite the better reproduction of the solution profile due to this scaling issue. This indicates that, given further normalization of inputs and outputs, the model may be able to extrapolate to mesh sizes larger than the training data, which would allow the training process to be sped up substantially by training only on lower resolution data.

8.5 Runtime

One of the most attractive reasons to use machine learning for estimating the solution of the Poisson equation versus traditional methods is the promise of speedup. Table 4 outlines the wall-clock runtime of both the sub-models and the full model using single precision run on an Nvidia Titan V versus the multigrid solver run on 64 threads on a 32-core/64-thread AMD Threadripper 2990WX CPU. Note that the model architecture and weights were not changed compared to the results presented above and the accuracy of the model was not evaluated.

Grid size	# of trials	Multigrid	DBCNN (4 BC)	HPNN	Poisson CNN
64	200	0.0179	0.0235	0.0387	0.0676
100	200	0.0361	0.03090	0.0411	0.0802
200	200	0.1101	0.05436	0.07174	0.1475
500	100	0.8580	0.1980	0.4123	0.6435
1000	50	3.3701	0.5785	1.7981	2.4585
3000	20	45.6587	4.3136	13.969	18.8986

Table 4: Wall clock runtimes of the Multigrid solver versus the DBCNN, HPNN and Poisson CNN models (in seconds)

The results suggest that at the grid sizes the results of this principally investigated, the Poisson CNN model does not offer a speedup though both sub-models do. The Poisson CNN model begins to offer meaningful speedups around grid sizes approaching 500×500 , eventually building up to almost thrice the speed of multigrid at 3000×3000 . Though it can be argued that larger/more complex models with longer runtimes may be necessary to achieve good accuracy at the grid sizes where the CNN offers a speedup and that CPU and GPU wall-clock runtimes are not directly comparable, these results regardless show that our model has the potential to offer substantial speedups to solve the Poisson equation when facing a 'real-world' use case comparison scenario especially in light of the fact that the model is able to reproduce the solution profile even when predicting on meshes denser than previously encountered.

It is noteworthy that no hyperparameter optimization efforts were conducted – it is likely that by tuning the number of hyperparameters, by e.g. reducing the number of channels in the intermediate layers or the number convolution layers altogether, substantial speedups could be achieved while making little or no compromise in terms of the predictive accuracy of the model. The extreme similarity of many of the feature maps in the initial layers of the model is supportive of this possibility. Finally, by the virtue of the fact that our model was not programmed to take advantage of the 'Tensor Cores' on the Titan V GPU (which require half-precision operations and specific programming to properly utilize) which offer up to 110TFlops of performance as opposed to 13.8 TFlops of standard single-precision performance on this GPU per Nvidia [30], further very substantial speedups are possible by taking full advantage of quickly developing deep learning-specific hardware.

9 Conclusion

A CNN model to solve the 2D Poisson equation with Dirichlet BCs was developed based on the approach of splitting the problem into a homogeneous Poisson problem and four further Laplace problems with one inhomogeneous BC each. Training of the models was done on purely synthetic, random datasets that were

generated with the aim of replicating the smooth functions a Poisson solver would be expected to handle in real world use cases. In order to achieve good convergence during training, a novel loss function – the L^p integral loss – was developed and demonstrated to be superior for this task to the mean squared error.

The model developed permits estimating the solutions with pointwise deviations on the order of 20% even when performing inference on inputs that are materially different from both training and validation data, based on test cases with analytical solutions such as the Taylor-Green Vortex Pressure Field and RHS functions created from Fourier series with random coefficients. Comparison of the runtime performance of the model indicates that the runtime at the grid sizes used to generate results for this work is similar to that of multigrid, but theoretical speedups up to 3x were observed when using the model with larger inputs. In light of the model’s ability to capture key solution features (though currently with the wrong scale) even when encountering meshes denser than previously seen, our proposed model provides a solid foundation to substantially accelerate the solution of the Poisson equation via machine learning.

Based on the successes showcased in this work, in future work we intend to improve our model by incorporating the following features:

Predicting on larger, previously unseen meshes By fixing the scaling issue demonstrated in the predictions made by the model when encountering larger meshes than previously seen, the training time can be reduced substantially by training on smaller problems than the targeted mesh sizes. Given large enough speedups, this makes training separate application-specific models (e.g. for CFD) more viable, allowing a tradeoff of generality for accuracy with substantially shorter time investments.

Neumann and Robin BCs Neumann and Robin BCs play critical roles in CFD to implement e.g. symmetry in the flow but are not currently supported. Though these are typically implemented in iterative or direct solvers through simply modifying the relevant rows in the left hand side matrix, this is not possible for NNs. One possible approach is adopting a strategy similar to the one outlined in Section 3, but since the BCs must retain their respective types in the homogeneous problem as well, having multiple models to solve the homogeneous problem with each combination of BCs possible. The number of separate models can be minimized by grouping BC combinations that are identical under simple rotations or reflections.

Different grid spacings along each dimension Currently, the model has only been trained on meshes that have identical grid spacings in both spatial directions. Specifying different grid spacings across different directions is a very common practice in many applications, and this will be likely incorporated into the models presented by adding the different grid spacings as an input parameter supplied to the dense layers.

3D meshes All work in the project has been focused on less memory- and time-intensive 2D problems so far, but most problems of interest in CFD are 3D. It is not expected that vast architectural changes will be necessary for a 3D version of this work since most convolutions etc. can be easily made 3D, however the greater number of parameters and much larger inputs can make training difficult and more memory intensive, necessitating high levels of parallelization across GPUs. Moreover, for very large problems such as those that can be encountered in very high fidelity fluid dynamics simulations, a significant software development effort to parallelize the convolution operations across multiple GPUs spatially as opposed to across the batch dimension will be necessary.

10 Acknowledgements

This work was supported by a PhD studentship funded by the Department of Aeronautics, Imperial College London.

References

- [1] S. H. Lui, *Numerical Analysis of Partial Differential Equations*. John Wiley & Sons, Inc., 2011.
- [2] H. Lee and I. S. Kang, “Neural algorithm for solving differential equations,” *Journal of Computational Physics*, vol. 91, no. 1, pp. 110 – 131, 1990.
- [3] M. W. M. G. Dissanayake and N. Phan-Thien, “Neural-network-based approximations for solving partial differential equations,” *Communications in Numerical Methods in Engineering*, vol. 10, no. 3, pp. 195–201, 1994.
- [4] I. E. Lagaris, A. Likas, and D. I. Fotiadis, “Artificial neural networks for solving ordinary and partial differential equations,” *IEEE Transactions on Neural Networks*, vol. 9, 1998.
- [5] N. Smaoui and S. Al-Enezi, “Modelling the dynamics of nonlinear partial differential equations using neural networks,” *Journal of Computational and Applied Mathematics*, vol. 170, no. 1, pp. 27 – 58, 2004.
- [6] M. Baymani, A. Kerayechian, and S. Effati, “Artificial neural networks approach for solving stokes problem,” *Applied Mathematics*, vol. 01, pp. 288–292, 01 2010.
- [7] L. Jianyu, L. Siwei, Q. Yingjian, and H. Yaping, “Numerical solution of elliptic partial differential equation using radial basis function neural networks,” *Neural Networks*, vol. 16, no. 5, pp. 729 – 734, 2003. Advances in Neural Networks Research: IJCNN '03.
- [8] N. Mai-Duy and T. Tran-Cong, “Numerical solution of differential equations using multiquadric radial basis function networks,” *Neural Networks*, vol. 14, no. 2, pp. 185 – 199, 2001.
- [9] M. Kumar and N. Yadav, “Multilayer perceptrons and radial basis function neural network methods for the solution of differential equations: A survey,” *Computers & Mathematics with Applications*, vol. 62, no. 10, pp. 3796 – 3811, 2011.
- [10] M. Abadi, A. Agarwal, P. Barham, E. Brevdo, Z. Chen, C. Citro, G. S. Corrado, A. Davis, J. Dean, M. Devin, S. Ghemawat, I. Goodfellow, A. Harp, G. Irving, M. Isard, Y. Jia, R. Jozefowicz, L. Kaiser, M. Kudlur, J. Levenberg, D. Mané, R. Monga, S. Moore, D. Murray, C. Olah, M. Schuster, J. Shlens, B. Steiner, I. Sutskever, K. Talwar, P. Tucker, V. Vanhoucke, V. Vasudevan, F. Viégas, O. Vinyals, P. Warden, M. Wattenberg, M. Wicke, Y. Yu, and X. Zheng, “TensorFlow: Large-scale machine learning on heterogeneous systems,” 2015. Software available from tensorflow.org.
- [11] A. Paszke, S. Gross, S. Chintala, G. Chanan, E. Yang, Z. DeVito, Z. Lin, A. Desmaison, L. Antiga, and A. Lerer, “Automatic differentiation in pytorch,” 2017.
- [12] M. Raissi, P. Perdikaris, and G. E. Karniadakis, “Physics informed deep learning (part i): Data-driven solutions of nonlinear partial differential equations,” 2017.
- [13] L. Lu, X. Meng, Z. Mao, and G. E. Karniadakis, “Deepxde: A deep learning library for solving differential equations,” 2019.
- [14] X. Meng and G. E. Karniadakis, “A composite neural network that learns from multi-fidelity data: Application to function approximation and inverse pde problems,” *Journal of Computational Physics*, p. 109020, 2019.
- [15] Z. Long, Y. Lu, X. Ma, and B. Dong, “Pde-net: Learning pdes from data,” 2017.
- [16] M. Raissi, “Deep hidden physics models: Deep learning of nonlinear partial differential equations,” 2018.
- [17] M. Raissi, P. Perdikaris, and G. E. Karniadakis, “Physics informed deep learning (part ii): Data-driven discovery of nonlinear partial differential equations,” 2017.
- [18] S. Rudy, S. Brunton, J. Proctor, and J. Kutz, “Data-driven discovery of partial differential equations,” *Science Advances*, vol. 3, 09 2016.

- [19] P. Isola, J.-Y. Zhu, T. Zhou, and A. A. Efros, “Image-to-image translation with conditional adversarial networks,” 2016.
- [20] J. Tompson, K. Schlachter, P. Sprechmann, and K. Perlin, “Accelerating Eulerian Fluid Simulation With Convolutional Networks,” *ArXiv e-prints*, July 2016.
- [21] X. Xiao, Y. Zhou, H. Wang, and X. Yang, “A novel cnn-based poisson solver for fluid simulation,” *IEEE Transactions on Visualization and Computer Graphics*, pp. 1–1, 2018.
- [22] T. Shan, W. Tang, X. Dang, M. Li, F. Yang, S. Xu, and J. Wu, “Study on a poisson’s equation solver based on deep learning technique,” 2017.
- [23] F. John, *Partial Differential Equations*. Springer, 1982.
- [24] C. M. Bishop, *Pattern Recognition and Machine Learning*. Berlin, Heidelberg: Springer-Verlag, 2006.
- [25] L. N. Olson and J. B. Schroder, “PyAMG: Algebraic multigrid solvers in Python v4.0,” 2018. Release 4.0.
- [26] K. He, X. Zhang, S. Ren, and J. Sun, “Deep residual learning for image recognition,” 2015.
- [27] V. Dumoulin and F. Visin, “A guide to convolution arithmetic for deep learning,” 2016.
- [28] T. Authors, *tf.keras.layers.Conv2D — TensorFlow Core r2.0*, 2019.
- [29] T. Authors, *tf.keras.callbacks.EarlyStopping — TensorFlow Core r2.0*, 2019.
- [30] N. Corporation, *The World’s Most Powerful PC GPU Titan V*, 2019.
- [31] K. Jarrett, K. Kavukcuoglu, M. Ranzato, and Y. LeCun, “What is the best multi-stage architecture for object recognition?,” in *2009 IEEE 12th International Conference on Computer Vision*, pp. 2146–2153, Sep. 2009.
- [32] V. Nair and G. Hinton, “Rectified linear units improve restricted boltzmann machines,” vol. 27, pp. 807–814, 06 2010.
- [33] X. Glorot, A. Bordes, and Y. Bengio, “Deep sparse rectifier neural networks,” in *Proceedings of the Fourteenth International Conference on Artificial Intelligence and Statistics* (G. Gordon, D. Dunson, and M. Dudík, eds.), vol. 15 of *Proceedings of Machine Learning Research*, (Fort Lauderdale, FL, USA), pp. 315–323, PMLR, 11–13 Apr 2011.
- [34] D. P. Kingma and J. Ba, “Adam: A method for stochastic optimization,” 2014.

A Overview of Convolutional Neural Networks (CNNs)

Neural networks (NNs) are universal smooth function approximators that have the ability to handle high-dimensional spaces by learning from large amounts of data as outlined by Bishop [24]. They are capable of learning very complex relationships between datasets for purposes as diverse as regression, image classification and speech recognition. Since both the right hand side (RHS) f and the solution u of the Poisson equation are typically smooth functions and the problem is extensible to a finite yet unbounded number of dimensions, NNs are a good candidate among the common Machine Learning (ML) algorithms with respect to their capability to learn a mapping between f and u .

The operational principle of almost all supervised ML algorithms relies on ‘learning’ (i.e. optimizing) a set of weights \vec{w} such that, given pairs of inputs \vec{x} and targeted outputs \vec{t} , the output of the algorithm $\vec{y}(\vec{x}, \vec{w})$ matches \vec{t} . How well the output \vec{y} and the target \vec{t} match is usually measured by a *loss function* $L(\vec{y}, \vec{t})$. A common choice for L in single target regression problems is the Mean Squared Error (MSE):

$$MSE = \frac{1}{n} \sum_i^n (y_i - t_i)^2 \tag{21}$$

Thus, the objective may be summarized as

$$\underset{\vec{w}}{\operatorname{argmin}} L(\vec{y}(\vec{x}, \vec{w}), \vec{t}) \tag{22}$$

Building blocks which constitute NNs are typically called *layers*. The simplest layer is called the *dense* or *fully-connected* layer, which takes an input of fixed size \vec{x} , multiplies it with a weight matrix \mathbf{W} , adds a bias \vec{b} and finally applies a (typically nonlinear) function h known as an *activation function*:

$$\vec{y} = h(\mathbf{W}\vec{x} + \vec{b}) \tag{23}$$

Common choices for h are tanh, ReLU (i.e. $\max(0, x)$) and the logistic sigmoid. The choice of h can greatly affect the ability of the NN to learn a mapping. For example, using the logistic sigmoid (which has the output range $[0,1]$) as the activation of the final layer of an NN where the target dataset has the range $[-1,1]$ will result in very poor performance. For image processing tasks, ReLU was found to be the most effective activation function in various studies such as those by Jarett et al. [31], Nair and Hinton [32] and Glorot et al. [33].

Due to having a dense matrix \mathbf{W} among its weights, a dense layer is capable of only mapping data with fixed sizes to each other and, as the input and the output get large, requires an extremely large number of parameters – e.g. if we consider the case of mapping the RHS of the Poisson equation sampled on a 100×100 grid to the solution also on a 100×100 grid using an NN with a just single dense layer, the number of parameters would be c. 10^8 $[=(100 \times 100)^2]$, which is prohibitively expensive from the perspective of memory and computation time requirements.

These shortcomings of the dense layer are addressed to a large degree by the *convolutional* NN layer. Instead of a dense weight matrix, a convolution layer *convolves* the input with a kernel – the operation involves elementwise multiplication of a kernel-sized subset of the input with the kernel, summing the resulting array, (optionally) adding a bias parameter, applying an activation function and ‘sliding’ the kernel to another subset to perform the same operation as illustrated in Figure 21

In practice, each convolution layer will have multiple output channels and each output channel will have a number of filters (combinations of kernels and associated biases) equal to the number of input channels. Hence, the convolution layer will convolve the input channels with each output channel’s associated filters and sum the resulting arrays for each output channel as depicted in Figure 22. As a result, a convolution layer with e.g.

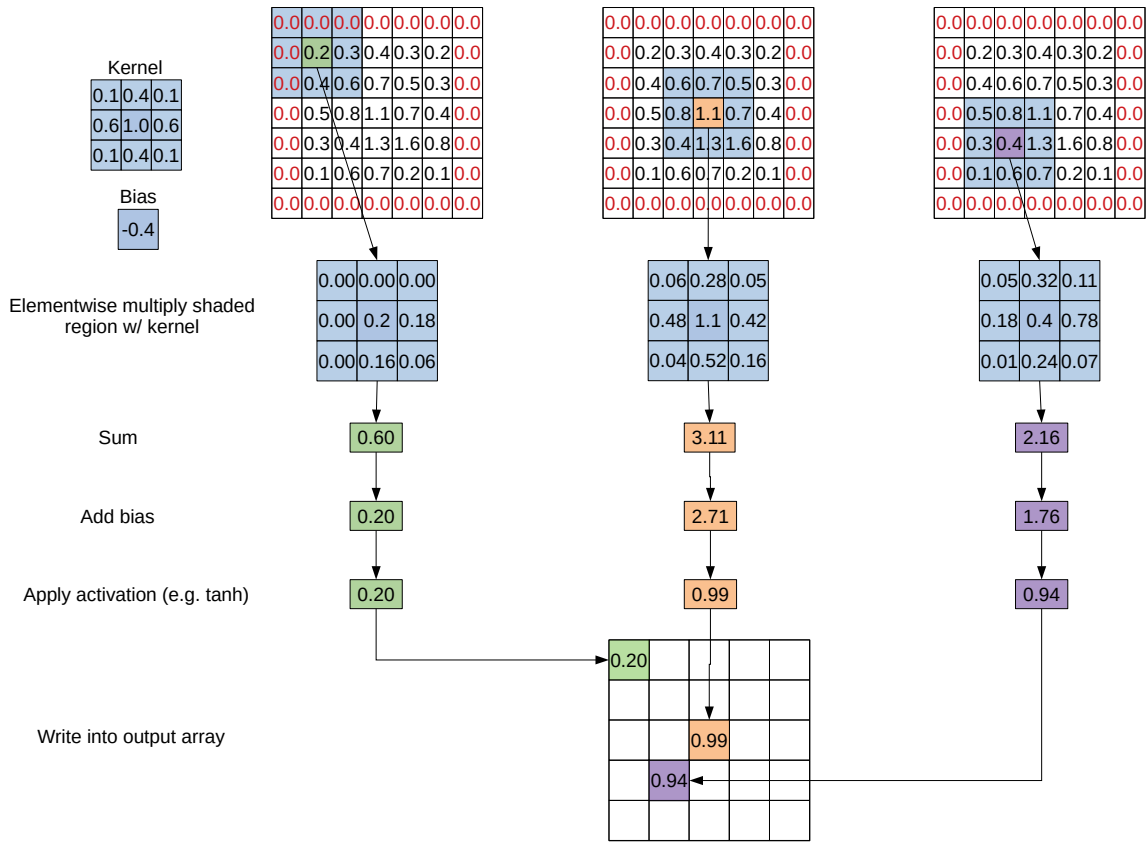


Figure 21: Illustration of the application of a 2D convolution on a 5×5 input with a 3×3 kernel. Red zeroes indicate padded values to retain the shape of the input.

a 5×5 kernel size and 16 output channels that takes photos as inputs (i.e. 3 input channels – red, green and blue) will have a kernel array of shape $[5, 5, 3, 16]$ and bias array of shape $[3, 16]$ for a total of 1248 parameters – 5 orders of magnitude fewer than the previous example using a single dense layer above.

One shortcoming of convolution layers is being able to propagate information in only a local manner – a 3×3 convolution kernel cannot modify its output in accordance with the bottom right pixel of a 100×100 input when processing the top left corner. One very common way of dealing with this problem is introducing *pooling* layers. Pooling layers reduce the size of the input by combining subsets of the inputs into a single value, typically through choosing the largest value or averaging. Figure 23 depicts a max pooling operation (with padding to ensure no part of the input is left out).

For the solution of the Poisson equation, pooling layers ensure that the CNN is able to capture information regarding the low-wavenumber modes that have periods larger than the largest convolution kernels used. Although an alternative method to deal with this problem would be simply using larger kernels, this leads to a very rapid rise in the number of parameters in the model which is undesirable as it substantially increases both training and prediction times as well as memory requirements.

Once the architecture is decided upon, typically as a certain arrangement of convolution, pooling and dense layers as well as more primitive operations such as summation of layer results, the next step is to train the NN to find the weights. The weights \vec{w} are typically found by using gradient descent-style algorithms such that

$${}^{k+1}\vec{w} = {}^k\vec{w} - \gamma \nabla_{\vec{w}} L(\vec{y}(\vec{x}, \vec{w}), \vec{t}) \Big|_{k, \vec{w}} \quad (24)$$

where pre-superscripts indicate iteration number, $\nabla_{\vec{w}}$ is the gradient operator with respect to the weights and γ is some scaling factor typically called *learning rate*. In practice this simple version of the algorithm, known

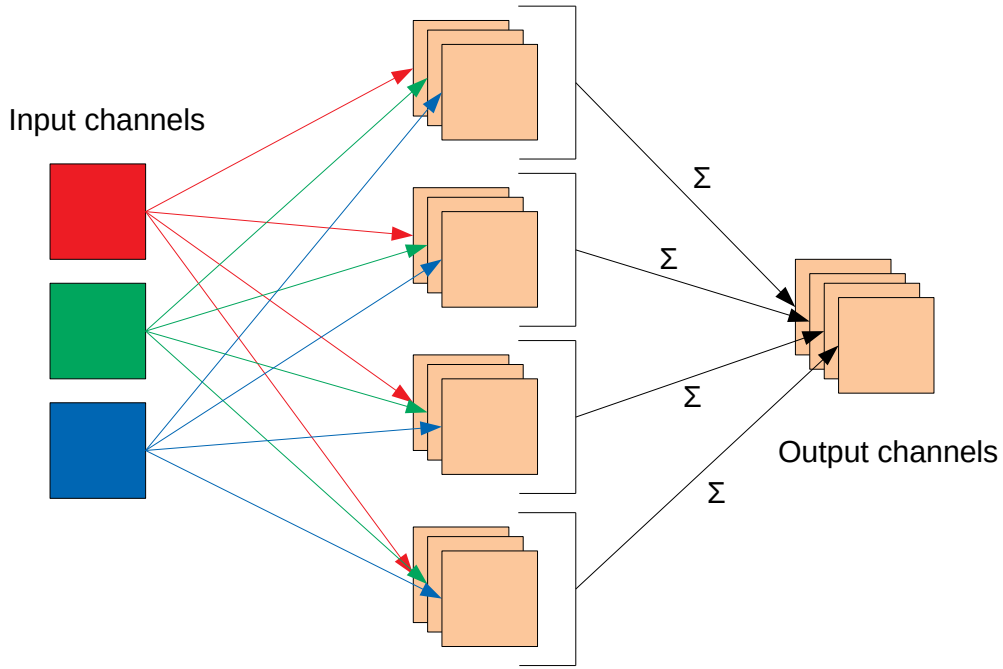


Figure 22: Operation of a convolution layer with 3 input and 4 output channels

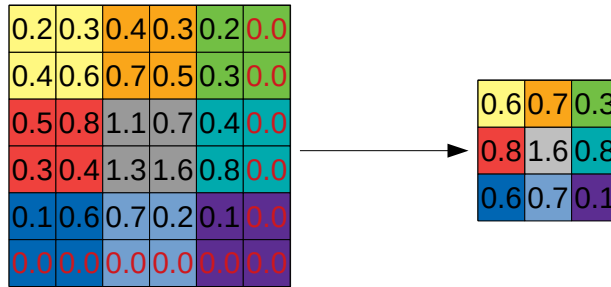


Figure 23: Max pooling operation with a $(2,2)$ pool size. The maximum value in each shaded region in the input is copied into the corresponding slot in the output.

as Stochastic Gradient Descent (SGD), is used less commonly in modern applications when training NNs than variants such as *Adam* (Adaptive Moment Estimation, by Kingma and Ba [34]) which dynamically updates γ to speed up the learning process or 'momentum' methods which set the direction of the weight update as a linear combination of the current gradient and previous gradient(s) to reduce the oscillatory behaviour of SGD.

Whether using SGD or one of its variants, the difficulty lies in computing the gradients $\nabla_{\vec{w}} L(\vec{y}(\vec{x}, \vec{w}), \vec{t}) \Big|_{k, \vec{w}}$ to update the weights. A simple approach to compute these values would be perturbing the weights one by one and applying a finite difference approximation, however this requires $O(n_{\text{weights}})$ operations for each data point in the training set, which is intractable for large models containing hundreds of millions of weights. Instead, the gradients are computed using the *backpropagation* algorithm, which simply is the successive application of the chain rule.

As an example case, if we consider an NN composed of two dense layers, using Equation 23 and denoting the

output of the i th layer as \vec{z}_i such that $\vec{z}_i = h_i(\mathbf{W}_i \vec{z}_{i-1} + \vec{b}_i)$, we can write the output as

$$y = h_2(\mathbf{W}_2 h_1(\mathbf{W}_1 \vec{x} + \vec{b}_1) + \vec{b}_2) = h_2(\mathbf{W}_2 \vec{z}_1 + \vec{b}_2) \quad (25)$$

To find the loss gradients with respect to the weights $\partial L / \partial \mathbf{W}$ (where $\mathbf{W} = [\mathbf{W}_1 \vec{b}_1 \mathbf{W}_2 \vec{b}_2]$), we can now apply the chain rule:

$$\frac{\partial L}{\partial \mathbf{W}_2} = \frac{\partial L}{\partial y} \frac{dy}{d\mathbf{W}_2} \quad (26)$$

$$\frac{\partial L}{\partial \vec{b}_2} = \frac{\partial L}{\partial y} \frac{dy}{d\vec{b}_2} \quad (27)$$

$$\frac{\partial L}{\partial \mathbf{W}_1} = \frac{\partial L}{\partial y} \frac{dy}{d\mathbf{W}_1} = \frac{\partial L}{\partial y} \frac{\partial y}{\partial z_1} \frac{dz_1}{d\mathbf{W}_1} \quad (28)$$

$$\frac{\partial L}{\partial \vec{b}_1} = \frac{\partial L}{\partial y} \frac{\partial y}{\partial z_1} \frac{dz_1}{d\vec{b}_1} \quad (29)$$

Since terms such as $\frac{\partial L}{\partial y}$ are merely partial derivatives, they can be computed analytically from the definition of the (user-chosen) function. Hence, to evaluate the gradients of the loss function we need to merely evaluate the loss while keeping track of the partial derivatives as information propagates from the input layer to the output layer (forward propagation) and then apply the chain rule first to the final layer to compute the derivatives and then use the derivatives we found for the final layer to compute the derivatives in the penultimate layer and so forth until we have all derivatives (backpropagation). Once we obtain all of the gradients, we can update the weights using Equation 24. This allows the loss function gradients with respect to the weights to be evaluated in a single forward-pass plus one backpropagation step, whereas finite differences would require $O(n_{weights})$ forward passes. Machine learning libraries typically handle this process automatically using autodifferentiation.